Fabrication and Characterizations of Fe/NaCl/Fe Magnetic Tunnel Junctions

by

Yuantao Ji

A thesis

presented to the University of Waterloo

in fulfillment of the

thesis requirement for the degree of

Master of Applied Science

in

Electrical and Computer Engineering

Waterloo, Ontario, Canada, 2015

Author's Declaration

I hereby declare that I am the sole author of this thesis. This is a true copy of the thesis, including any required final revisions, as accepted by my examiners.

I understand that my thesis may be made electronically available to the public.

Abstract

The tunneling magnetoresistance (TMR) of magnetic tunnel junctions (MTJ) was discovered in the middle of the last century, and it has attracted many researchers' attention and led to a revolution in the field of data storage and magnetic sensing technologies over the past two decades.

There are different methods of fabricating the magnetic tunnel junctions. The industry tends to use the sputtering method at room temperature, which is more time and cost effective. While in laboratories researchers tend to use high vacuum electron-beam deposition system or Molecular Beam Epitaxy system (MBE) to grow the layers at elevated temperatures to make them epitaxial.

The basic structure of the magnetic tunnel junctions has two ferromagnetic electrode layers separated by a thin insulation barrier layer. Currently most industry is using cobalt-iron alloys as the ferromagnetic electrodes and magnesium oxide as the insulation layer. The most famous and profitable industrial products with this technology are non-volatile data storage and readout devices used in magnetic random access memory (MRAM) and hard disc drives.

In this thesis, high vacuum electron-beam deposition system is used to grow Fe/NaCl/Fe magnetic tunnel junctions on Si (100). We found that epitaxial tunnel junctions were prone to pinholes and electrode oxidation which severely reduced tunneling magnetoresistance. The highest tunneling magnetoresistance achieved in this system was on polycrystalline tunnel barriers with a 0.7nm thin Mg layer insertion, the tunneling magnetoresistance of which was 22.3% at room temperature and 37.8% at 77K in liquid nitrogen.

Acknowledgements

The author would like to thank Prof. Guo-Xing Miao for his supervision, and Qiang Li, Yongchao Tang, Lin Li, and Zhiwei Gao for their collaborations. The author would also like to thank Prof. David Cory and his team members for their assistance on this project.

Table of Contents

Abstract iii
Acknowledgements iv
List of Figures vi
List of Tables viii
Nomenclature ix
Chapter 1 1
1.1 Motivation 1
1.2 Objective 5
1.3 Thesis Organization 6
Chapter 2 7
2.1 Spintronics 7
2.2 Magnetic Tunnel Junctions 8
2.3 Tunneling Magnetoresistance 9
2.4 Applications of Spintronics 15
Chapter 3 19
3.1 Calculations of transport and magnetic properties of Fe/NaCl/Fe MTJs 19
3.2 Layer by layer growth of NaCl on FeO (100) 23
3.3 Fabrication of NaCl Barriers MTJ 27
Chapter 4 30
4.1 High vacuum e-beam and thermal evaporation system 30
4.2 Sample preparation 31
4.3 Measurement 35
Chapter 5 37
5.1 Epitaxial growth of NaCl on Fe (100) 37
5.2 Characterizations of Fe/NaCl/Fe MTJs with MgO insertion 39
5.3 Selected results of other samples 42
Chapter 6 44
References 46

List of Figures

Figure 1.1. 1 Applications of magnetic tunnel junctions. 1
Figure 1.1. 2 Evolution of Magnetoresistance 2
Figure 1.1. 3 The structure of the magnetic tunnel junctions 3
Figure 1.1. 4 Illustration of the rock-salt structure of NaCl 4
Figure 1.1. 5 The Bloch states Wave Function Symmetry and its decay rates 4
Figure 2.2. 1 The structure of magnetic tunnel junctions 9
Figure 2.3. 1 The magnetization versus external magnetic field of ferromagnets. 10
Figure 2.3. 2 Three schemes of MTJs 12
Figure 2.3. 3 TMR of Fe/MgO/Fe MTJs (a) MR curve (b) MR vs thickness 13
Figure 2.3. 4 Conductance of double-barrier magnetic tunnel junctions 14
Figure 2.3. 5 Spin filter tunneling. 15
Figure 2.4. 1 Spin-torque diode 16
Figure 2.4. 2 Spin logic TMR junctions 17
Figure 3.1. 1 The structure of Fe/NaCl/Fe MTJs 20
Figure 3.1. 2 Total energy, interface magnetic moment of 4Fe/NaCl/Fe junction 20
Figure 3.1. 3 Layer resolved DOS of Fe/NaCl/Fe 21
Figure 3.1. 4 Layer resolved charge transfer and magnetization of NaCl MTJ 22
Figure 3.1. 5 Conductance and TMR vs magnetic slab of the barrier layer 23
Figure 3.2. 1 NaCl film on FeO deposit at (a) 120℃, (b) 145℃ and (c) 175℃ 24
Figure 3.2. 2 Structure of 4 ML NaCl on FeO 25
Figure 3.2. 3 Structure of NaCl (12 ML) film on FeO 26
Figure 3.2. 4 NaCl (4 ML) deposited at 90℃ directly on (a) Fe (001) (b) FeO 26
Figure 3.3. 1 XRD scan of MgO (001) substrate/Fe (5 nm)/NaCl (10 nm) 27
Figure 3.3. 2 M–H curve for the Fe/NaCl/Fe structure at room temperature 28
Figure 3.3. 3 The MR curve and IV curve for the Fe/NaCl/Fe MTJ 29
Figure 4.1. 1 The structure of High vacuum e-beam/thermal evaporation system 30
Figure 4.1. 2 Schematic structure of shadow mask 31
Figure 4.2. 1 Wafer etch 32
Figure 4.2. 2 MgO (100) buffer layer on Si (100) 32
Figure 4.2. 3 Growth of Fe (100) bottom electrodes 33
Figure 4.2. 4 Mg insertion 33
Figure 4.2. 5 Definition layer 34
Figure 4.2. 6 NaCl Barrier layer 34
Figure 4.2. 7 Fe top electrode layer 35

Figure 4.3. 1 The schematic diagram of measurement. 35
Figure 4.3. 2 The schematic diagram of measurement in liquid nitrogen. 36
Figure 5.1. 1 XRD θ-2θ scan of MTJ without Mg insertion. 37
Figure 5.1. 2 Off-axis φ scan on the Fe (110) reflections. 38
Figure 5.2. 1 XRD θ-2θ scan of the Mg inserted MTJ. 39
Figure 5.2. 2 Tunneling magnetoresistance measured at room temperature 40
Figure 5.2. 3 The I-V characteristics of the magnetic tunnel junction 41
Figure 5.2. 4 Tunneling magnetoresistance ratio vs bias voltage 41

List of Tables

Table 4.3. 1 The selected results of the epitaxial growth of NaCl on Fe 42
Table 4.3. 2 The selected results of the Fe/NaCl/Fe junctions.....43

Nomenclature

Abbreviations

TMR	Tunneling Magnetoresistance
MTJs	Magnetic Tunnel Junctions
MRAM	Magnetic Random Access Memory
DOS	Density of States
ASLD	All Spin Logic Devices
FWHM	Full Width at Half Maximum
STM	Scanning Tunneling Microscopy

Symbols

μ	Magnetic moment
ħ	Planck's constant
m_e	Mass of electron
q	Elementary electric charge
R_p	Resistance of parallel state of MTJ
R_{ap}	Resistance of anti-parallel state of MTJ

Chapter 1

Introduction

1.1 Motivation

Since Meservey and Tedrow [1] first discovered the phenomenon of spin-polarized tunneling in the 1970s, it has led to revolution in the data storage and magnetic sensing technologies over the past two decades [2]. Many applications have been developed along this direction (see Figure 1.1), especially after the significant improvement of the ultra-high (giant) tunneling magnetoresistance (TMR) [3,4,5].

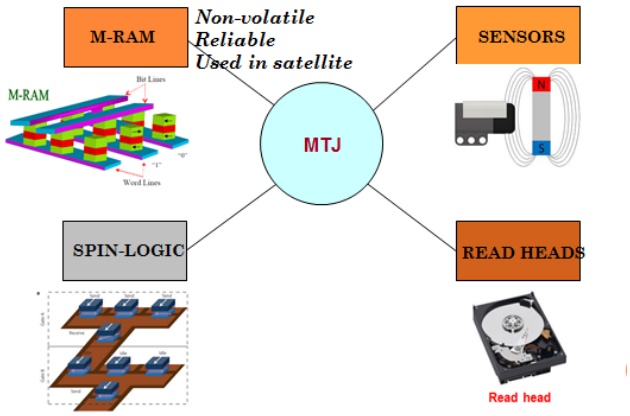

Figure 1.1. 1: Applications of magnetic tunnel junctions (MTJs). For example, MTJs can be used as highly sensitive magnetic sensors, as non-volatile memory units in magnetic random access memory (MRAM), as logic gates in spin current driven logic devices, and as read heads in the hard disk drives.

The MRAM, made of MTJs, is considered to be the next generation of the RAM.

Compare to dynamic random access memory (DRAM), MRAM is non-volatile which means the data will not lose if the power is off. In addition, the spintronic nature of these memory cells allows them to consume nearly two orders of magnitude less power than DRAM cells. MTJs are also suitable to make sensors and read heads of hard drive. Spin logic devices maybe the next generation of logic devices. Compared to pure CMOS (complementary metal–oxide–semiconductor) technologies, the spin logic devices have built-in memory as well as significantly reduced power consumption, allowing digital processors to finally overcome the "power wall" obstacle and reach faster clock speed.

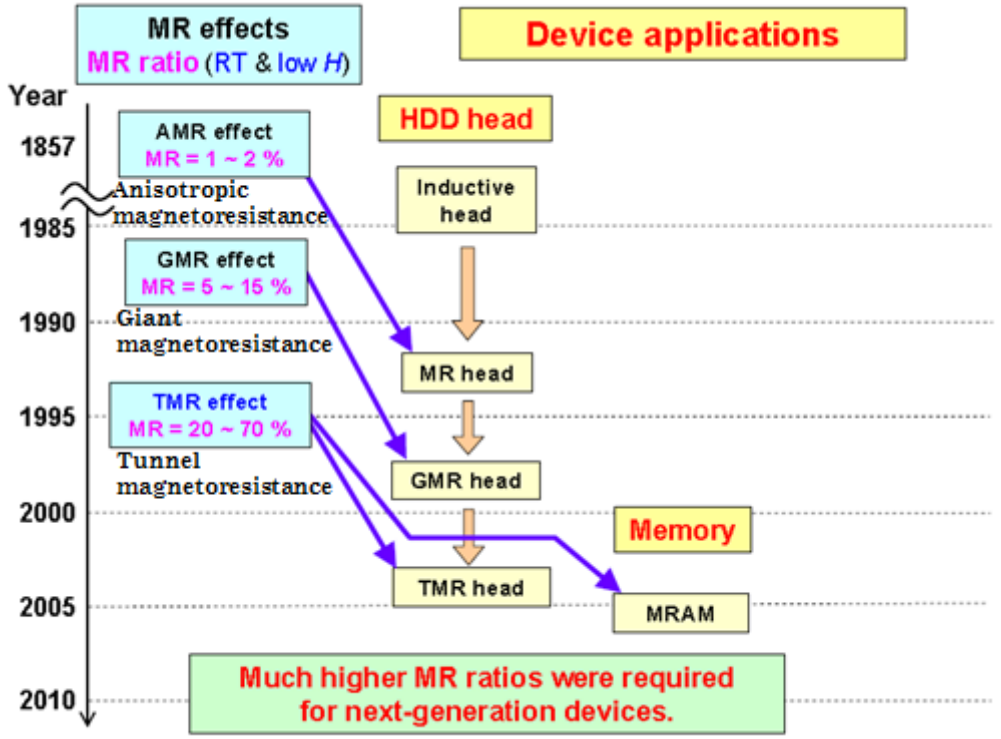

Figure 1.1. 2 Evolution of Magnetoresistance

In the middle of 19th century, the phenomenon of anisotropic magnetoresistance (AMR) was discovered which shows only 1-2% MR ratio at room temperature. MR ratio is the relative change of the device resistance under applied magnetic fields. In the 1980s and 1990s, the giant magnetoresistance and the tunnel magnetoresistance effects were discovered which significantly improved the MR ratio to beyond 10% at room temperature, and resulted in immediate commercialization of the products. With

the MR ratio continuously being improved, devices based on the MR technologies will become more efficient and develop into even broader range of applications.

The basic structure of magnetic tunnel junctions contains two ferromagnetic layers separated by an ultra-thin insulation barrier layer [4]. The current industry is using CoFeB as the ferromagnetic electrodes and magnesium oxide as the insulation layer (see Figure 1.2). They have been widely used in non-volatile data storage technologies such as memory units in MRAM and read heads in hard disc drives.

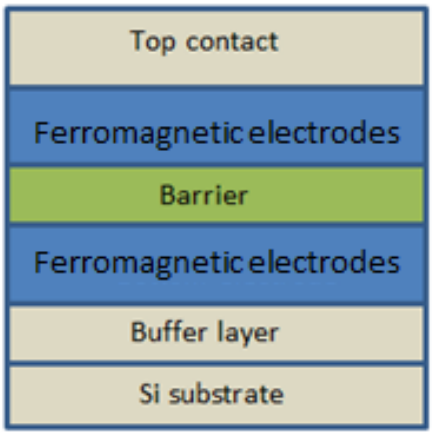

Figure 1.1. 3: The structure of the magnetic tunnel junctions

Butler et al. [6] theoretically showed that TMR of epitaxial Fe/MgO/Fe (001) magnetic tunneling junctions should be higher than 1000% due to the conservation of Bloch state symmetry of the tunneling electrons during the tunneling process. Experimentally, over 600% MR ratio has been reported on MgO based MTJs at room temperature [4], proving the validity of the coherent tunneling process. Using a similar theory, Vlaic et al. [7] have calculated that TMR of epitaxial Fe/NaCl/Fe (001) MTJs should also be higher than 1000%, and similar results have been developed by Tao et al. [8] in FePt/NaCl/FePt (001) tunnel junctions.

To choose a right material as the barrier layer, the material should ideally be rock-salt structured and lattice matching with Fe or CoFe to promote coherent Bloch state tunneling, containing only light elements to prevent spin scattering, in addition to being electrically insulating. There are only a small number of compounds satisfying these criteria, and NaCl is one of the most promising candidates.

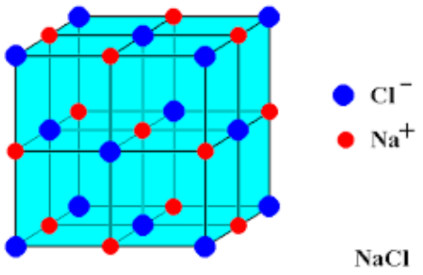

Figure 1.1. 4 Illustration of the rock-salt structure of NaCl

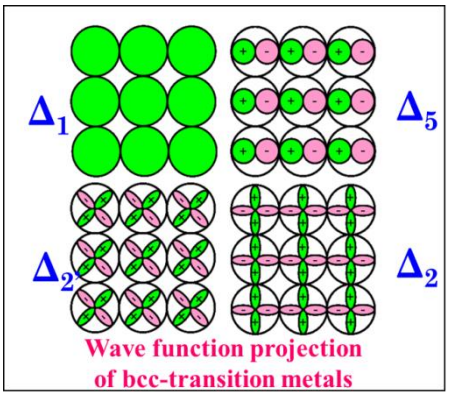

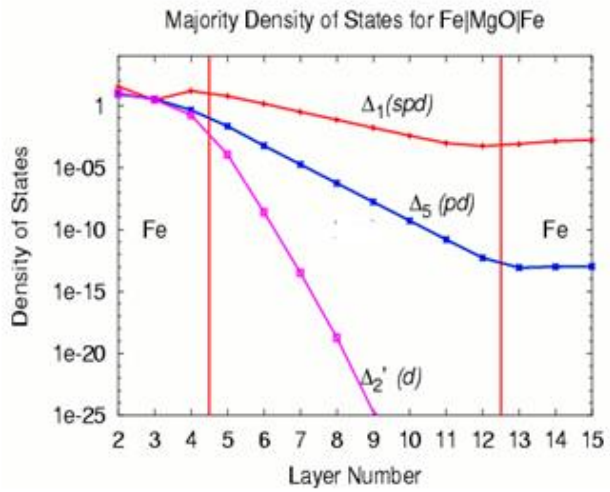

Figure 1.1. 5 Projection of different Bloch states from bcc-Fe onto the tunnel barrier (upper panel) and their corresponding decay rates within rock-salt structured MgO tunnel barrier (lower panel). + and – signs on the colored wave function lobes indicate opposite phases [6].

There are 4 types of Bloch states with most relevance: Δ_1, Δ_2, Δ_2', and Δ_5 states (Figure 1.1.4). The decay rates of them are different inside the tunnel barrier. In epitaxial bcc-Fe/MgO system, Δ_1 states decay the slowest within the barrier and dominate the tunneling process, and they are fully spin-polarized. Therefore MgO is a suitable material to form the barrier layer. The next contributor, Δ_5 states, are only partially spin-polarized. Though most of them are exponentially filtered out, the rest still leads to a finite conductance in the antiparallel configuration.

Since the band structure and crystal structure of sodium chloride are quite similar to those of magnesium oxide [9,10,11], we expect sodium chloride can be epitaxially grown on Iron. It is therefore a suitable material to form the barrier layer of magnetic tunnel junctions to establish coherent tunneling [12,13,14,15,16,17]. Additionally, because sodium chloride contains only light elements, similar to the most popular barrier materials aluminum oxide [18] and magnesium oxide [3,4], it will not generate much spin scattering inside the barrier therefore it can offer better spin transport efficiency [19,20].

Furthermore, since bcc-Fe/NaCl system has different amount of Δ_1 and Δ_5 states compare to bcc-Fe/MgO system, we can discover more about the coherent tunneling phenomena, especially roles of the non- Δ_1 bands in the modified barriers.

In this thesis, we report the fabrication of Fe/NaCl/Fe magnetic tunnel junctions under various growth conditions and their magnet transport results.

1.2 Objective

The objective of this research is to demonstrate and enhance the tunneling magnetoresistance in Fe/NaCl/Fe magnetic tunnel junctions towards room temperature applications. We have explored and optimized the conditions of the epitaxial growth of NaCl on Fe, and investigated their effects on the device performance as well as compared the differences between traditional MTJs (Fe/MgO/Fe) and NaCl barrier MTJs.

1.3 Thesis Organization

Chapter 2 introduces the background knowledge of spintronics, magnetic tunnel junctions and tunneling magnetoresistance.

Chapter 3 reviews some existing research of the Fe/NaCl/Fe MTJs. Including the calculation and experiment about the NaCl barrier MTJs.

Chapter 4 illustrates the detailed experimental methods to fabricate the NaCl barrier MTJs in this thesis.

Chapter 5 demonstrates the results and the discussion of the experiments.

Chapter 6 introduces the future work of the experiment.

Chapter 2

Background

In this chapter, the background knowledge of spintronics, magnetic tunnel junctions and tunneling magnetoresistance will be introduced.

2.1 Spintronics

Spintronics is a rising technology in solid state electronic devices. It combines benefits from the intrinsic electron spins, the resultant magnetic moments, and the fundamental electronic charges [21,22].

The phenomenon of spin-dependent electron transport was discovered in the 1970s. The phenomenon of giant magnetoresistance (GMR) was first observed by Albert Fert et al.[23] and Peter Grünberg et al. [24], and tunneling magnetoresistance was first observed by M. Jullière in 1975 [25].

The angular momentum of an electron contains two main components. One is the spin angular momentum which is intrinsic to electrons. The other one is the orbital angular momentum because of the orbital motion of electrons. The magnitude of the spin angular momentum along an arbitrary direction is $0.5\hbar$ because the quantum number of electron's spin is 1/2. Because of the half-integer spin quantum, electrons act as Fermions [26]. Similar to orbital angular momentum of charged particles generating magnetic moments, the electron spin angular momentum also creates a

magnetic moment with the magnitude as in equation 2.1.1, and its projection in a given direction is therefore one Bohr magneton (μ_B).

$$\mu = \frac{\sqrt{3}}{2}\frac{q}{m_e}\hbar \tag{2.1.1}$$

The spins of a large amount of electrons can collectively affect the magnetic and electronic properties of materials, such as giving the materials permanent magnetic moments like in ferromagnets. In general, the number of spin up and spin down electrons are equal. A spintronic device relies on the generation and manipulation of spins for information processing. The polarization of spin dependent property X is defined in equation 2.1.2.

$$P_X = \frac{X_\uparrow - X_\downarrow}{X_\uparrow + X_\downarrow} \tag{2.1.2}$$

The spin polarization can be achieved by creating a splitting between spin up and spin down energy bands. For example, one can apply a large magnetic field to a material which creates the Zeeman Effect [27] or spin pumping to drive the system into non-equilibrium [28]. The time period of maintaining the non-equilibrium spin population is known as the spin lifetime τ. The electrons in a typical metal have an extremely short spin lifetime (normally much less than 1 ns), and many researchers are working in this field to extend the spin lifetime by using lighter elements and perfecting the materials growth. There are different mechanisms for the decay of spin polarized population, most of them are related to spin flip scattering or spin dephasing. [29].

2.2 Magnetic Tunnel Junctions

The Magnetic Tunnel Junctions typically have 3 layers as the core components. The top and the bottom layers are ferromagnetic electrodes. In the middle is the thin barrier layer (typically a few nanometers) consisting of some dielectric material (See Figure 2.2.1).

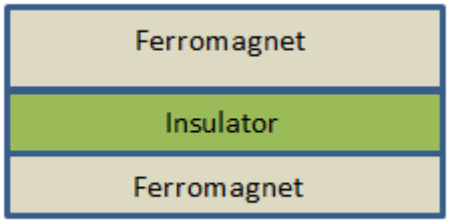

Figure 2.2. 1: The structure of magnetic tunnel junctions

There are different methods of fabricating the magnetic tunnel junctions. The industry tends to use the sputtering method, which is cheaper and more time efficient. While in laboratories researchers tend to use high vacuum electron-beam deposition system or Molecular Beam Epitaxy system to make the system epitaxial. In this thesis, we fabricated Fe/NaCl/Fe magnetic tunnel junctions using high vacuum electron-beam deposition system.

2.3 Tunneling Magnetoresistance

Tunnel magnetoresistance is a phenomenon that happens in magnetic tunnel junctions. An applied external magnetic field can control the magnet direction of the two ferromagnetic layers separately. If the spin orientations of the two ferromagnetic layers are parallel, it is easier for electrons to tunnel through the insulating barrier than in the antiparallel state. Therefore, the resistance of the junction shows two states (low or high), which is known as tunnel magnetoresistance (See Figure 2.3.1).

The TMR ratio is defined in equation 2.3.1:

$$\mathrm{TMR} = \frac{R_{ap} - R_p}{R_p} \tag{2.3.1}$$

R_{ap} is the resistance of the magnetic tunnel junction when the magnetic fields of the two ferromagnetic electrodes are antiparallel, while R_p is the resistance of the parallel state.

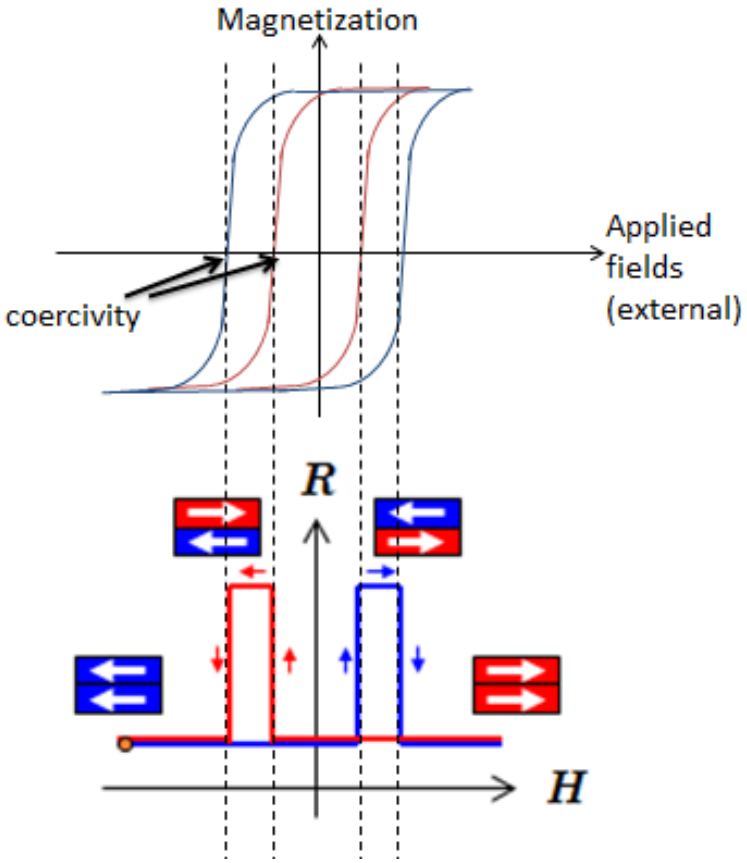

Figure 2.3. 1 the top picture is the magnetization versus external magnetic field of two different ferromagnets. Coercivity is the value of external magnetic field at which the magnetization changes sign. The coercivity can be changed by changing the thickness of the layers. If the coercivities of the two ferromagnetic layers are different, an antiparallel state can be achieved in certain field windows (the bottom picture).

Julli ère et al. [25] have quantified the TMR phenomenon with the spin polarization of ferromagnetic electrodes. The spin polarization P of an electrode is related to the spin dependent density of states (DOS) defined as D in equation 2.3.2.

$$\mathrm{P} = \frac{D_{\uparrow}(E_f) - D_{\downarrow}(E_f)}{D_{\uparrow}(E_f) + D_{\downarrow}(E_f)} \qquad (2.3.2)$$

In general, if the electrons' spin orientations are parallel to the magnetization direction, they are in the spin up state. The orientations of the spin-down electrons are opposite to the magnetization direction. Then the TMR ratio can be expressed as equation 2.3.3. P_1 and P_2 are the spin polarization of the two ferromagnetic electrodes.

$$\mathrm{TMR} = \frac{2P_1P_2}{1 - P_1P_2} \tag{2.3.3}$$

There are always some electrons tunneling through the barrier layer. The numbers of electrons traveling in both directions are the same at equilibrium. When a positive bias voltage is applied on the MTJ, the electrons tend to tunnel to the positive electrode. The total current can be split into 2 components, one is spin up current and the other is spin down current. The two channels' conductance are different depending on the magnetic state of the MTJ. [30,31]. Normally TMR decreases when the bias voltage increases or the temperature increases. We see from 2.3.3 that if the spin polarization of both electrodes (P_1, P_2) are both 100%, the TMR will become infinity.

Symmetry filtering is another major development in TMR. Initially, epitaxial Si, Ge, GaAs and ZnSe [32] were proposed. The tunnel matrix is different when the incoming electrons' Bloch wave functions are different. Then the Fe/MgO/Fe epitaxial systems were predicted [6,16] and achieved [3,4]. The mechanism of the large TMR is due to the presence of efficient symmetry filtering.

Figure 2.3.3 shows some Bloch states of 3d transition metals in the (100) direction. Electrons with Δ_1 symmetry have the smallest decay rate and Δ_1 state is 100% polarized. For Fe electrodes, there are no Δ_1 states in the minority spin channels. For MgO, only electrons with Δ_1 states can easily tunnel through but no available states are present in the counter electrode in the antiparallel alignment. Therefore the TMR of MgO MTJs is very high. While the NaCl barrier contains some Δ_5 states which is not 100% polarized and has a larger decay rate. Therefore the TMR of NaCl barrier is slightly lower [7].

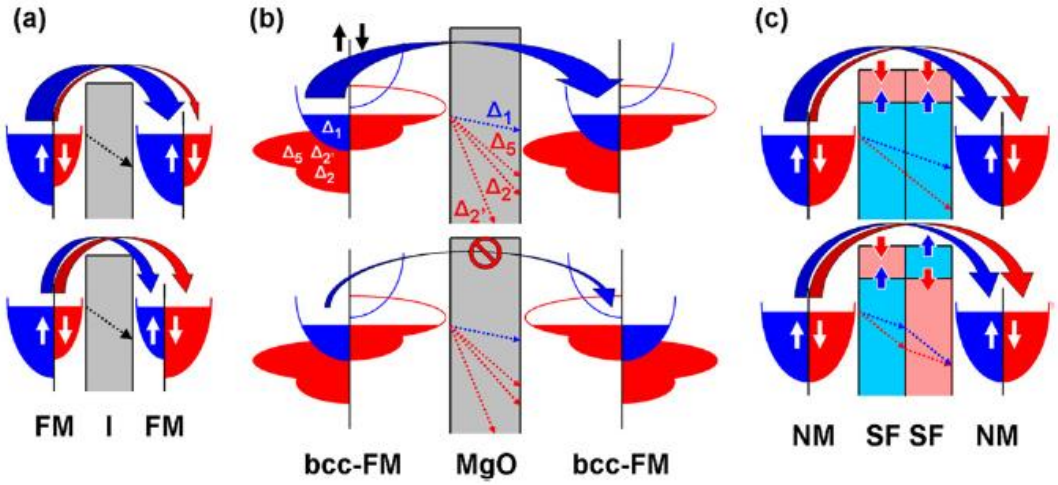

Figure 2.3. 2 three schemes of MTJs [30]. The top panels are the parallel state and the bottom panels are the antiparallel state. (a) shows a normal energy barrier, in which the decay rates of tunnel electrons are the same. The spin-DOS will determine the TMR. The TMR increases when the spin polarization is higher. (b) is a symmetry filtering barrier. In epitaxial junctions the decay of tunnel electrons are different if their Bloch states are different. The Δ_1 Bloch states have the highest transmission coefficient in Fe/MgO/Fe. While in NaCl there are some Δ_5 Bloch state [7], the expected TMR is slightly lower. (c) is a spin-filtering barrier. Initially the electrons have no spin polarization. Because of the spin dependent barrier heights, the tunnel electrons can be filtered in the barrier. The barriers' spin-filtering efficiency will determine the TMR.

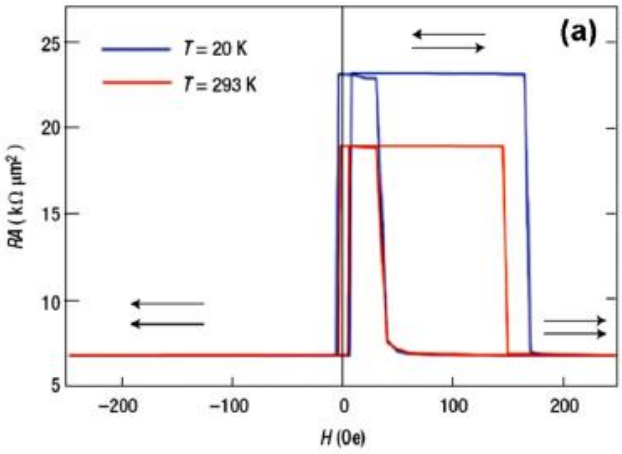

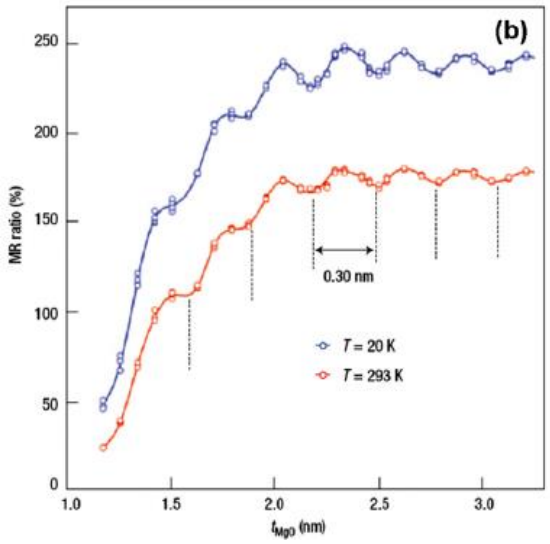

Figure 2.3. 3 TMR of epitaxial Fe/MgO/Fe MTJs (a) MR curve (b) MR vs thickness [4]

The TMR is related to the thickness of MgO barrier. When the thickness is less than 2nm the TMR will decrease. Cr insertion can be used to improve the impedance of the junctions [33]. There are no Δ_1 states in Cr on the Femi level. The symmetry of the electrons can be changed by non-specular scattering. Eliminate the defects such as Mg and O vacancies in MgO can also change the resistance of the MTJs. [34]

Double-barrier junctions can also control coherent tunneling process. A quantum well state is formed in the double MgO barrier MTJs [35]. The junction conductance shows quantum oscillation with respect to the applied bias voltage. TMR can be improved when inserting a Fe quantum well between Cr and MgO layer. [36,37]

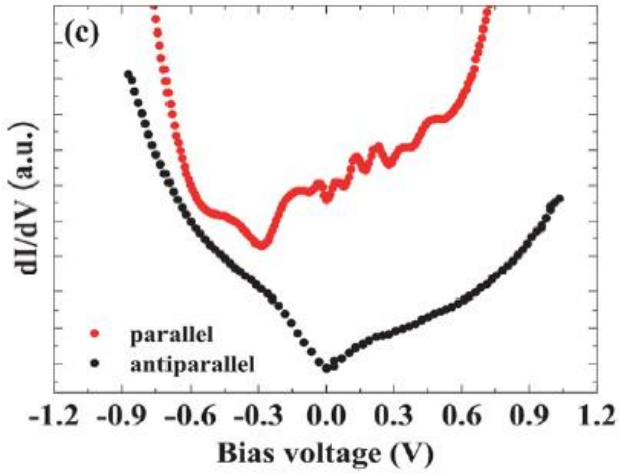

Figure 2.3. 4 Conductance of parallel and antiparallel states of double-barrier magnetic tunnel junctions (in nm) Fe (50)/MgO (2)/Fe (1.5)/MgO (2)/Fe (15) [35]

There are many methods to improve the TMR in this type of MTJs. The introduction of amorphous electrodes [38] and the optimization of the barrier layer growth conditions are important considerations. The epitaxy correlation between the barrier layer and electrodes is also important. Post annealing after deposition of materials can greatly improve the TMR. Furthermore, the surface sensitivity of the tunneling process will add some difficulty to the processing. The first few layers will determine the effectiveness of the spin tunneling process. One challenge in the MTJ fabrication process is to avoid the oxidation of the bottom electrodes. FeO formed at the interface will affect the conductance mediated by Δ_1 bands. Mg insertion is a suitable way to solve the problem [39]. One can insert an ultra-thin Mg layer between the bottom electrode and the MgO barrier to prevent Fe from oxidation.

Spin filtering is yet another way to allow the creation of spin filter tunnel junctions. The tunnel currents' spin polarization is directly related to the tunneling probability through the barrier. Figure 2.3.5 illustrates the tunneling process of a spin filter. Because of the different barrier heights, the spin up and spin down electrons have different tunneling probabilities. The minority spin will be filtered out. Hence, spin filtering can act as a spin source. [40]

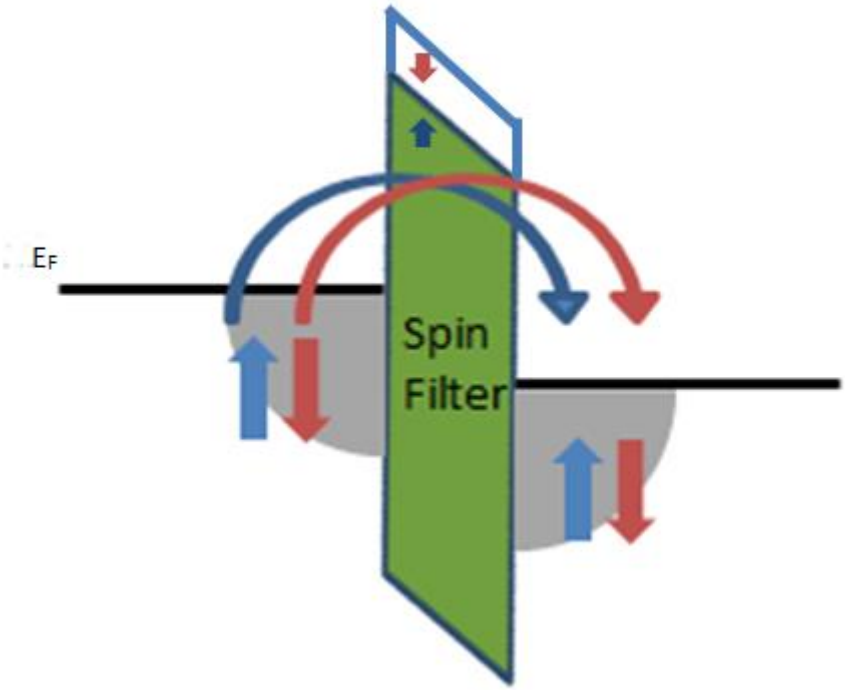

Figure 2.3. 5 spin filter tunneling. The conduction band of the barrier is split; the barrier heights and transmission probabilities are different.

2.4 Applications of Spintronics

There are many industrial applications of TMR. Most of the current read heads in hard disk drives are based on the TMR technologies. They can precisely read out the data at storage density over 500GB/$inch^2$. The storage units become faster and more compact due to the improvement of the TMR ratio and switching speed.

TMR can also be used in magnetic sensing, programmable spin-logic units, and non-volatile data storage such as MRAM. Magnetic random access memory is a nonvolatile memory device. The data can be stored with the magnetization directions. The speed and density of MRAM is close to DRAM while the MRAM is also

non-volatile because the magnetic elements stably retain their directions at ambient conditions. Because there is no need to constantly refresh the data, MRAM also enjoys significantly reduced power consumption. MRAM has both the capabilities of hard discs and RAM which are fast and non-volatile, respectively.

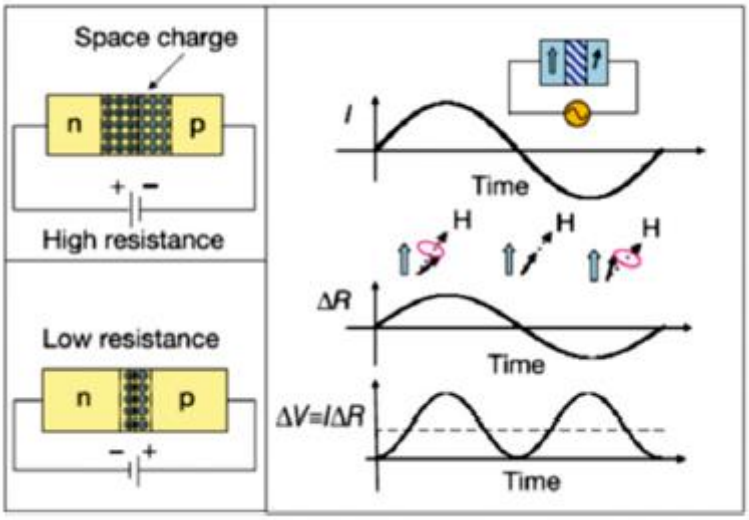

Figure 2.4. 1 spin-torque diode; the schematic diagram of p–n junction, the polarity of the applied voltage bias will affect the resistance of the junction and the thickness of the depletion layer. [41]

Spin-transfer torque is a phenomenon that the orientation of the magnetic layer in MTJ can be changed by spin-polarized current [42]. A spin-torque diode can act as diode if the TMR ratio of MTJs is large enough. If the free layer of a magnetic tunnel junction is driven near its FMR frequency, the electrons will rotate in phase with the applied ac current. In the first half cycle of ac voltage, the spins will rotate in larger angle because of the external magnetic field. And in the second half cycle the rotation angle is smaller. The resistance of the junction is higher in the first cycle, then become lower in the next half cycle. Therefore it will generate a DC output at the input of an AC current. [41]

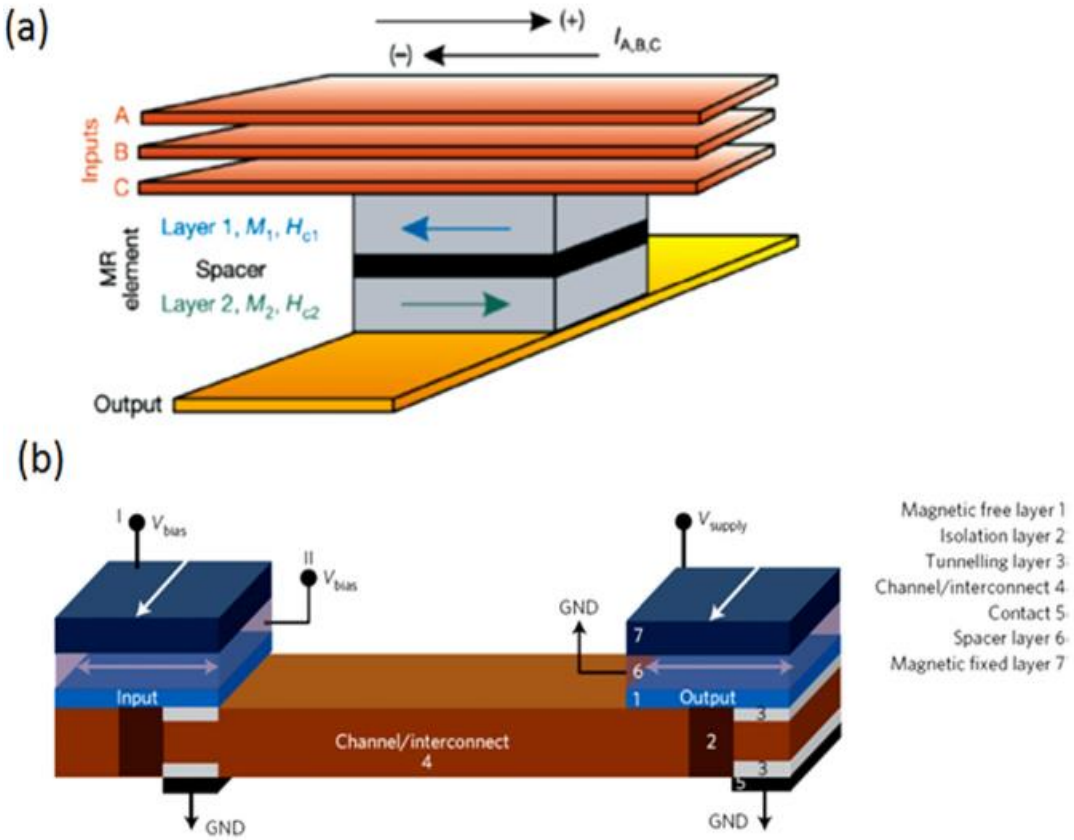

Figure 2.4. 2 spin logic TMR junctions. (a) a programmable spin-logic unit (b) all-spin logic device (ALSD). [43,44]

The figure above shows two logic devices based on spins. (a) is the schematic diagram of a programmable spin-logic unit which may be used for reprogrammable computing in the future. We can change the orientations of the magnetic layers by selectively varying some independent field lines. In figure (a), the input of 0 and 1 can be defined by applying +I and –I. The 0 and 1 for output can represent high and low resistance respectively. The logic operations (and/or) can be achieved by changing the magnetization orientation of M_1 layer while the magnetization orientation of M_2 is fixed to + direction.

(b) shows the concept of an all-spin logic device (ALSD). It uses spin current to do the operations. Every unit of the device can generate spin current for output or receive spin current for input. When a large current is introduced to the top layer and

flows out from the middle layer, a neutral position will be achieved in the free layer by spin-transfer torque effect. When the voltage is off, its final direction will be determined by the spin current inside the channel. It can operate as AND/OR logic devices. Compared to the traditional devices, the all-spin logic device has its own build in memory therefore it saves power and has better scalability [44].

Chapter 3

Literature Review

This chapter will introduce the existing research results on Fe/NaCl/Fe based MTJs including the available calculations and experiments in the literature.

3.1 Calculations of transport and magnetic properties of Fe/NaCl/Fe MTJs

Vlaic et al. [7] have calculated the transport properties of Fe/NaCl/Fe using Kubo–Landauer formalism transmission matrix formulation [45].

$$G_X^\sigma = \frac{e^2}{h}\frac{1}{N}\sum_k \int dE\left(\frac{-df(E)}{dE}\right)T_X^\sigma(k,E) \tag{3.1.1}$$

The e^2/h is the quantum conductance. N is the number of k points in the surface Brillouin zone. *f*(E) is the equilibrium Fermi–Dirac distribution function. $T_X^\sigma(k,E)$ is the transmission coefficient of magnetic state X.

The geometry of Fe/NaCl/Fe is as Figure 3.1.1.

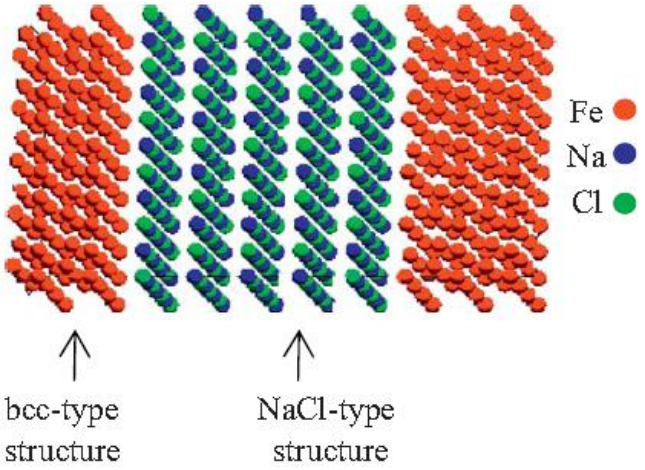

Figure 3.1. 1 the structure of Fe/NaCl/Fe MTJs [7]

In the above supercell, the Fe is bcc structure and NaCl is rock salt-type which means all lattice constants are matched $a_{NaCl} = 2a_{Fe}$. The calculation of total energy showed that minimum energy was achieved at the lattice constant a_o = 2.75 Å (Figure 3.1.2) rather than the experimental value Fe (2.86 Å). Therefore a_o = 2.75 Å was used in the following calculations. Figure 3.1.2 (b) shows the increase of the magnetic moments of the interfacial Fe layers over the bulk values.

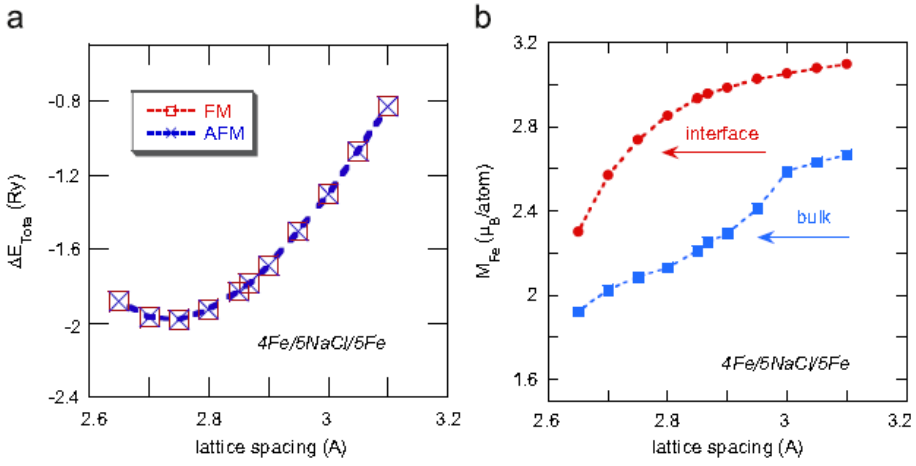

Figure 3.1. 2 Total energy, interface iron magnetic moment and exchange coupling of 4Fe/NaCl/Fe junction [7]

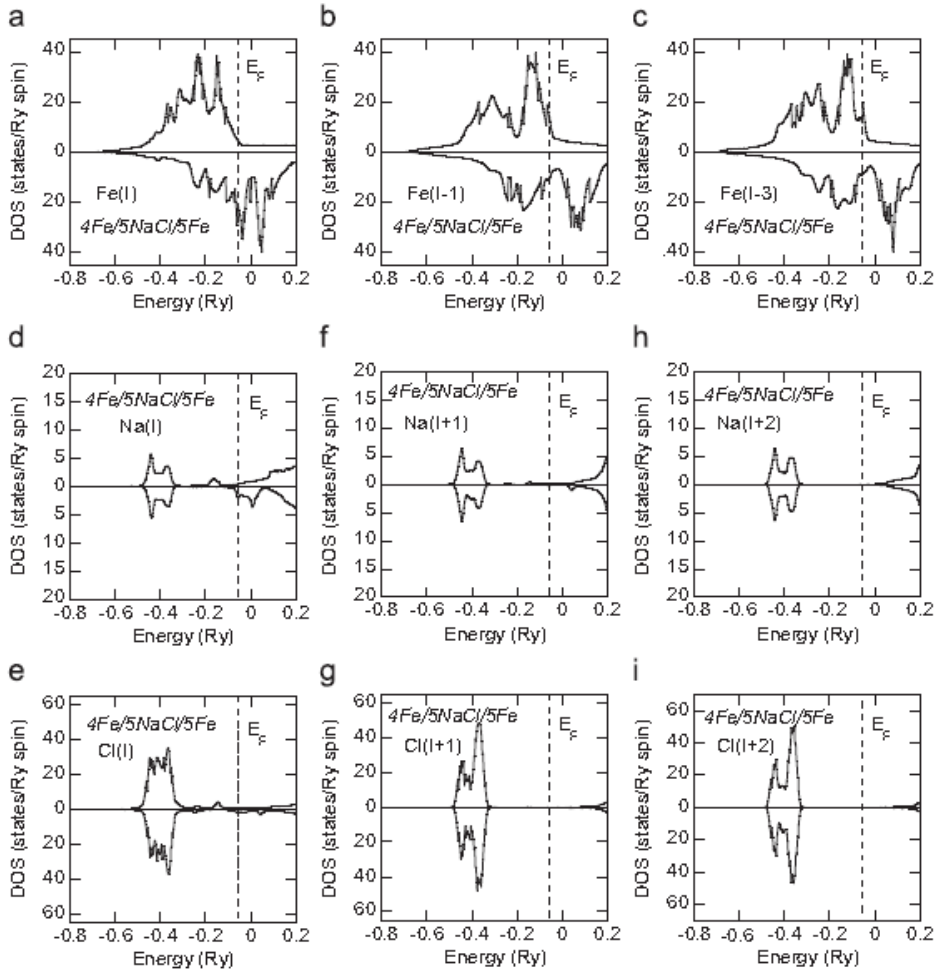

Figure 3.1. 3 Layer resolved DOS of Fe/NaCl/Fe [7]

The figure above shows the layer resolved DOS for Fe/NaCl/Fe. The DOS is bulk-like when it is not at the interface. At the Fermi energy the majority spin DOS of the Fe is increased while the minority spin DOS is decreased. And a sharp peak is just above the Fermi level.

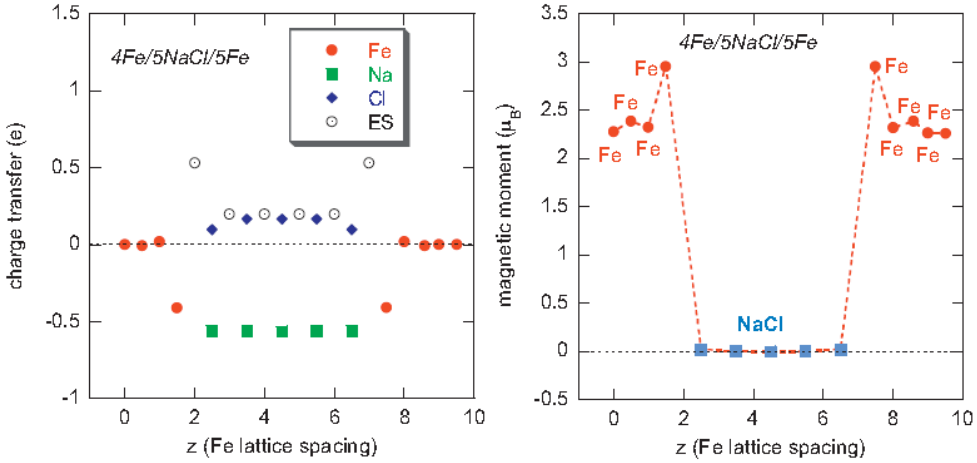

Figure 3.1. 4 layer resolved charge transfer and magnetization profile of NaCl MTJ [7]

From Figure 3.1.4, it can be observed that significant charge transfer occurs between the interfacial layers. At the interface, the charge of iron atoms decreases by about 0.41e while the charge of NaCl layer increases about 0.09e. The magnetic moment of the iron atoms which are not at the interface tends to have a bulk-like behavior while the iron atoms at the interface have larger magnetic moment which is similar to Fe/MgO interfaces [46].

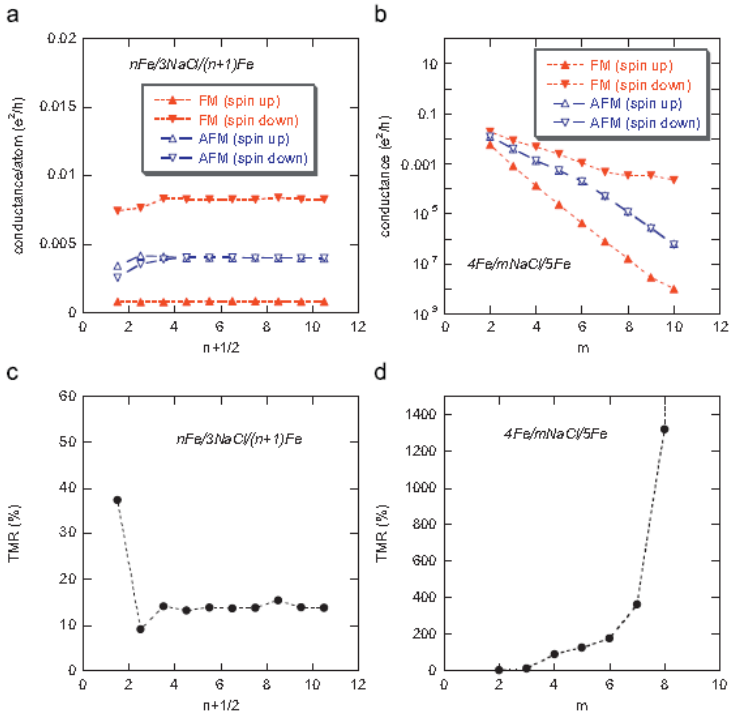

Figure 3.1. 5 Conductance and TMR vs magnetic slab and the thickness of the barrier layer [7]

The thickness of the NaCl insulating layer significantly affects the conductance. When the thickness increases the TMR will increase rapidly due to enhanced symmetry filtering over distance.

3.2 Layer by layer growth of NaCl on FeO (100)

NaCl thin films can be epitaxial grown on Fe (100) in ultra-high vacuum. Low energy electron diffraction is used to measure the surface properties of NaCl layer. When the temperature is below 145℃, it will form monoatomic thick islands and when the temperature is higher than 175℃ biatomic thick islands are present. So the NaCl turns out to be prone to pinholes when NaCl is directly grown on the Fe (100) substrate. However, when there is some oxygen on Fe, the NaCl grows layer by layer to form a flat thin film which is even better than MgO on Fe (100) [47].

The base pressure of this experiment is in the 10^{-11} mbar. Fe layer is grown by reduction of $FeCl_2$ using hydrogen reduction on Fe (100) substrate. After that the sample is annealed in 600℃. Pure oxygen is feed in the chamber to oxidize the Fe to form FeO. NaCl is grown on the FeO at 90–250℃. Non-contact atomic force microscopy (AFM) is used to measure surface properties at 300K (room temperature).

When NaCl is grown in temperatures at 120℃ it nucleates on the terraces. When the deposit temperature is 145℃ islands presents whose height is about 1.9Å. The shape is roughly square with preferential alignment of (110) directions with respect to the Si substrate. Some NaCl bilayers also nucleate at 4.2 Å height on the step edges of the FeO. When the temperature increases above 175℃ there are more nucleation. The NaCl unit cell is rotated by 45 degree to that of the substrate.

Figure 3.2.1 shows the different temperature during the NaCl deposition (2 monolayers (ML). When the sample is grown at 120℃ the surface will be covered with NaCl. However there are still some holes and islands. It is mostly layer-by-layer growth.

If the temperature is higher than 145℃ (the figures (b) and (c)), the islands near the step edge are higher than the NaCl layer. And there are dislocations which are usually along (110) direction. Figure (c) is at the step edges, the film is irregular when the temperature is higher than 145℃. Some regions are not integral number of monolayers, which means the orientation may change.

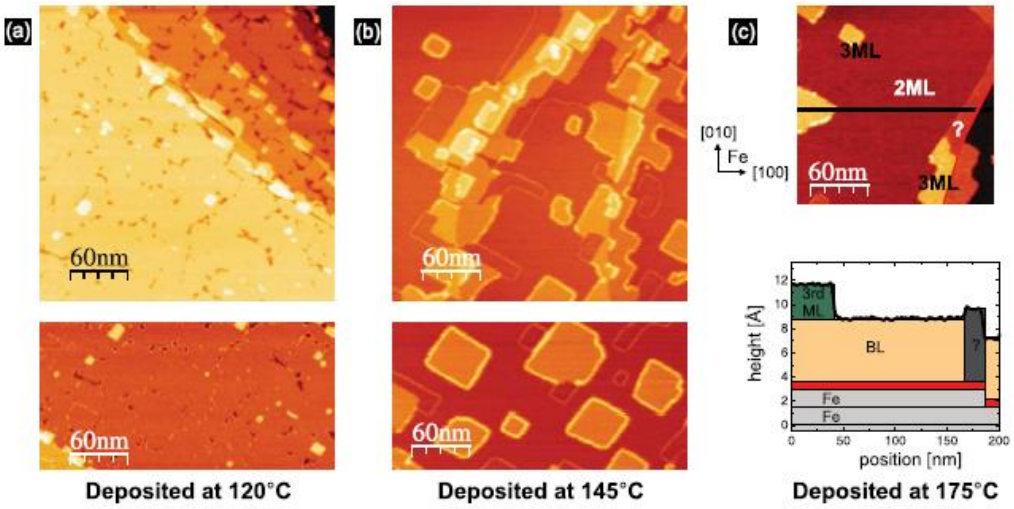

Figure 3.2. 1 NaCl film on FeO deposit at (a) 120℃, (b) 145℃ and (c) 175℃. (a) and

(b) shows terraces and islands. (c) top panel shows cross section of iron step edge and bottom panel shows schematic of the coverage at 175℃. [47]

Figure 3.2.2 (a) shows 4 monolayers of NaCl grown at 120℃. The third ML is completed, while the fourth ML is incomplete. And there are a few islands on the 5th ML. There are no dislocations in the structure of the first 2 ML, which indicates that the first 2ML grow successfully. The local contact potential difference (LCPD) map (Figure (b)) shows the complex pattern with local variations (68%). Figure (c) shows the forth ML island edges superimposed with the Kelvin probe force microscope (KPFM) image. Figures (d) and (e) illustrate the annealed sample (160℃). Specifically, the islands become larger while the LCPD contrast of the annealed sample becomes more uniform. There are fewer defects in the annealed film. Figure (f) shows the NaCl is rotated 45◦ to the substrate.

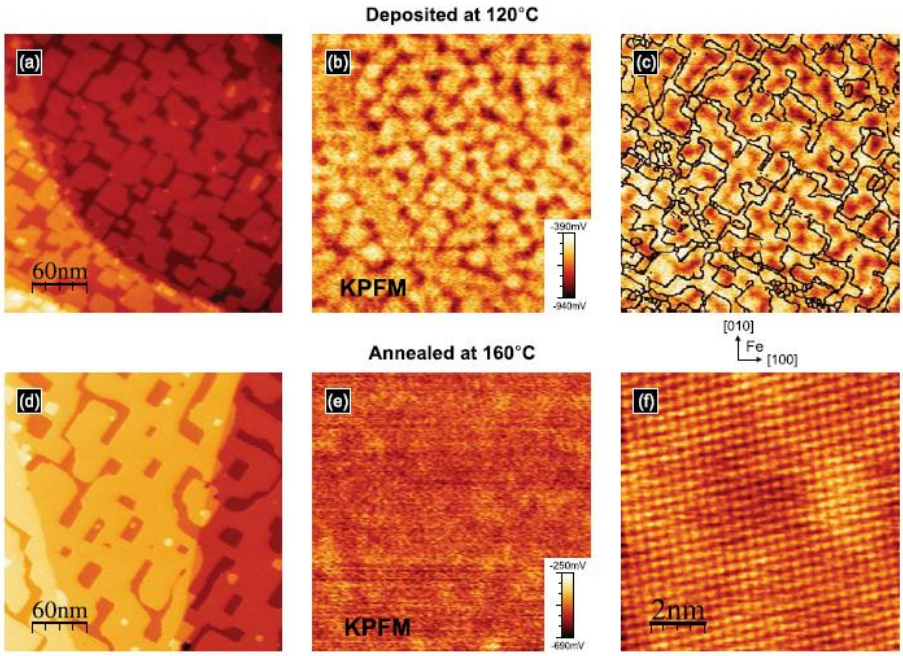

Figure 3.2. 2 Structure of 4 ML NaCl on FeO grown at 120℃ and annealed at 160℃. (a) and (d) are NC-AFM topography images, (b) and (e) are KPFM images and (c) shows the positions of island edges. (f) shows that the lattice is distorted, which means the NaCl unit cell is rotated by 45◦. [47]

Since the first 2 ML are successfully grown on the FeO, therefore this method is

suitable to fabricate NaCl on FeO substrates. Specifically, the film should be grown at a temperature higher than 120℃, and annealed at 160℃ for 2 hours. Then the best result was achieved (See Figure 3.2.3).

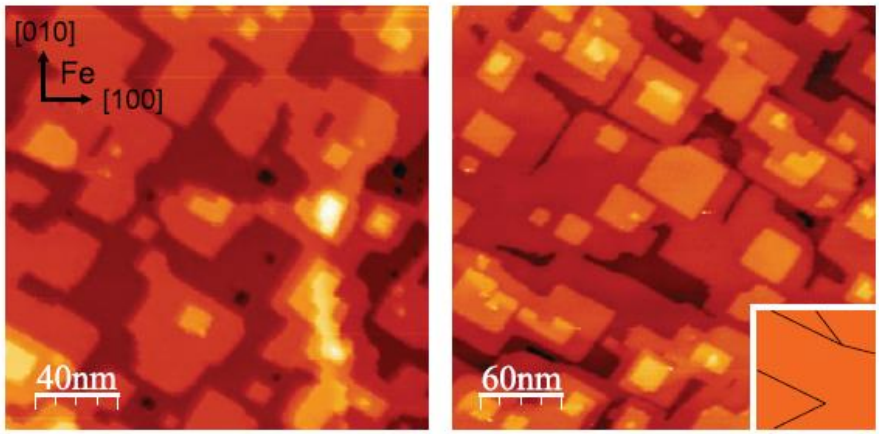

Figure 3.2. 3 Structure of NaCl (12 ML) film on FeO, successfully layer by layer grown at 120℃ and annealed at 160℃ for 2 hours. [47]

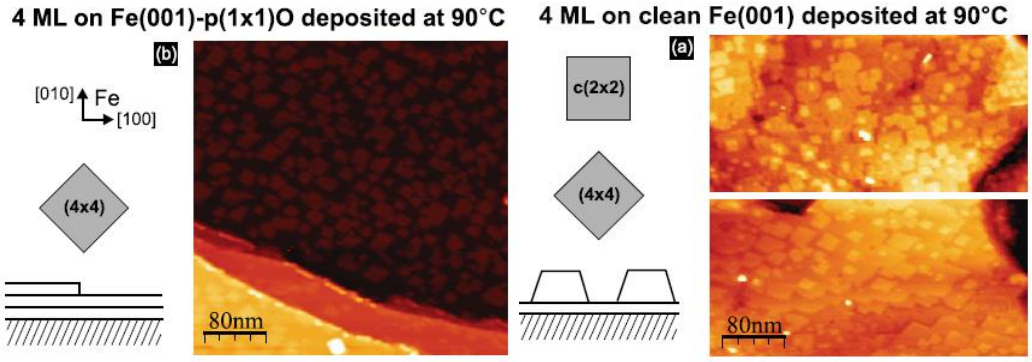

Figure 3.2. 4 NaCl (4 ML) deposited at 90℃ directly on (a) Fe (001) (b) FeO [47]

Oxygen is strongly bound to the iron atoms which provents oxygen from reacting with NaCl. Figure 3.2.4 shows 4 ML NaCl grown on Fe (001) and the FeO surface. The growth on Fe (001) substrate is like the Stranski–Krastanov mode (figure (a)). In addition two orientations are present on the sample. In contrast, NaCl on FeO showed the desired layer by layer growth (figure (b)).

3.3 Fabrication of NaCl Barriers MTJ

Nakazumi et al. [48] first reported fabrication of Fe/NaCl/Fe MTJs. The NaCl barrier was epitaxially grown on Fe (100) using high vacuum deposition system with shadow masks. The top Fe electrode is polycrystalline. TMR of the junction is 3% at room temperature and the junction current–voltage characteristics is non-linear.

In this experiment, the base vacuum is better than 10^-8 Torr. The bottom Fe electrode is 50nm and is grown at room temperature and then annealed at 500℃. The NaCl barrier layer is 10nm and also annealed at 500℃ which significantly reduces the full width at half maximum (FWHM) of the Fe (200) and NaCl (200) peaks in XRD, indicating improved structural quality. Finally, 150nm Fe layer is deposited on top followed by 100nm silicon dioxide to prevent oxidation and moisture. The growth rate of all the layers are 0.3Å/s.

Figure 3.3.1 shows the XRD of a sample with: MgO (001) substrate/Fe (5 nm)/NaCl (10 nm). Fe (002) and NaCl (002) peaks can be observed clearly which means the orientation of Fe and NaCl are both (001).

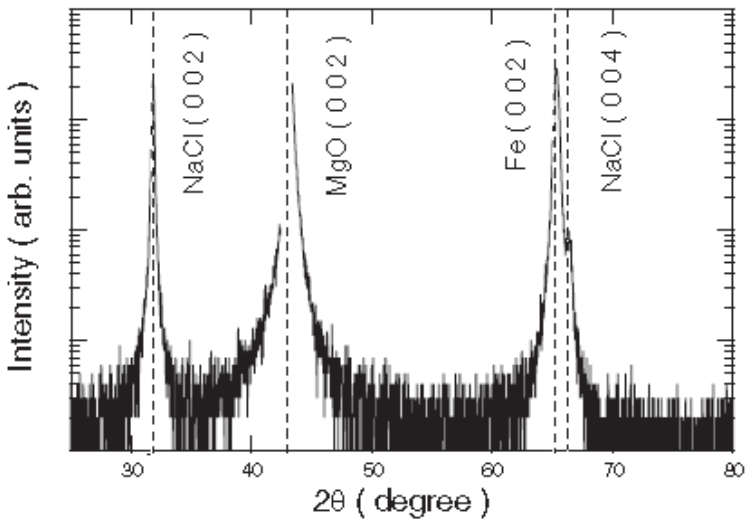

Figure 3.3. 1 XRD scan of MgO (001) substrate/Fe (5 nm)/NaCl (10 nm) [48]

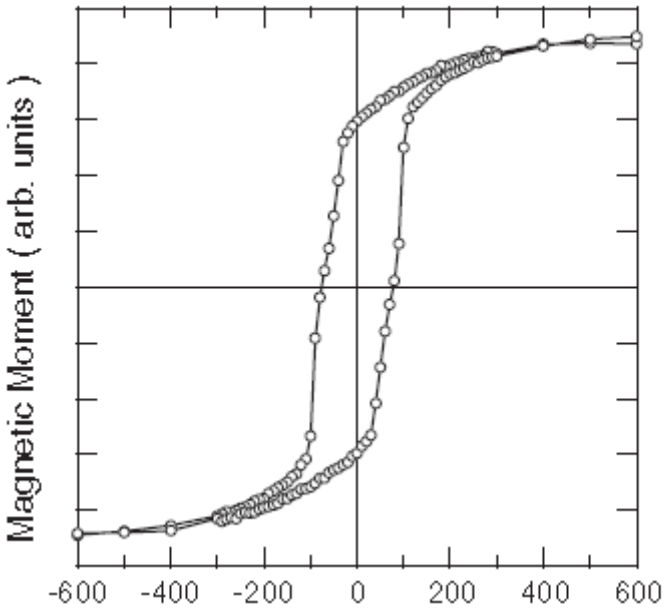

Figure 3.3. 2 M–H curve for the Fe/NaCl/Fe structure at room temperature [48]

Figure 3.3.2 is the magnetization versus external magnetic field (M–H) curve of a NaCl MTJ at room temperature. The external magnetic field was applied parallel to the in-plane easy axis of the bottom Fe (001) epitaxial thin film. The inflection points at the middle of the loop indicate that the layers' coercivity are different and the magnetization of the two ferromagnetic electrodes rotate separately.

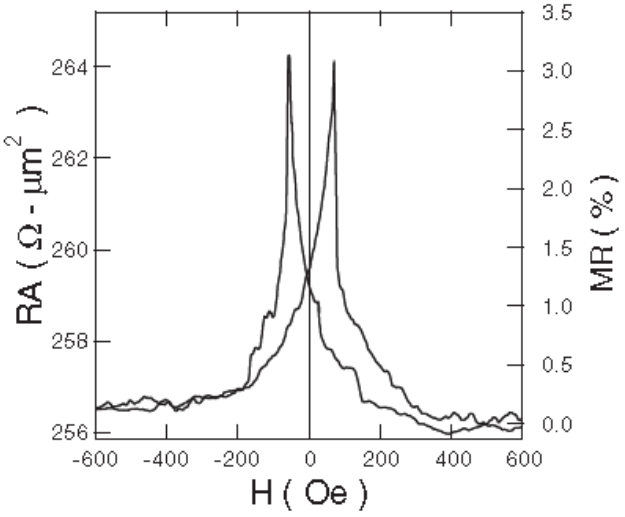

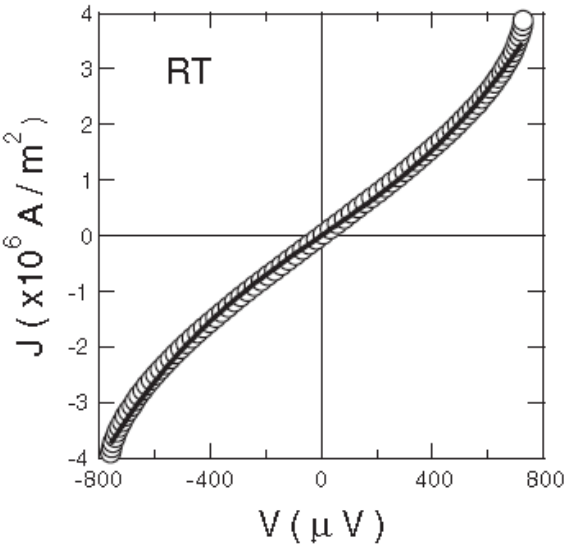

Figure 3.3. 3 The MR curve and IV curve for the Fe/NaCl/Fe MTJ at room temperature [48]

The MR curve is measured with 1mA current and the MR ratio is about 3% at room temperature. The magnetic fields at the maximum MR point are around the inflection points of the M–H curve in Fig. 3.3.2 which indicates that the MR arose from a spin-valve-like effect rather than from bulk effects MR (such as anisotropic MR).

The IV curve in Figure 3.3.4 is non-linear which means it is the tunneling mechanism that dominates the transport properties. It is similar to the MgO barrier magnetic tunnel junctions. The TMR mainly depends on the interfacial magnetism therefore the presence of FeCl at the interface may reduce the TMR. The TMR ratio might be improved with further optimization on the growth processes.

Chapter 4

Experimental

This chapter will introduce the detailed experimental methods to fabricate the NaCl barrier MTJs in this thesis.

4.1 High vacuum e-beam and thermal evaporation system

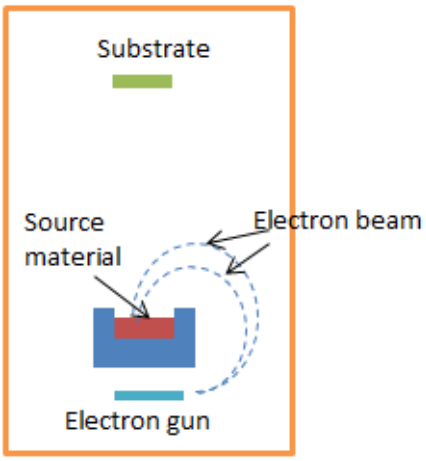

Figure 4.1. 1 the structure of High vacuum e-beam/thermal evaporation system

The high vacuum e-beam and thermal evaporation system is used to deposit the NaCl MTJs in this thesis. The e-gun filament is made of tungsten which can produce a narrow, collimated electron beam which has high kinetic energy when accelerated by a high voltage. The electron beam will strike the source material and result in a very high temperature, which makes the material vaporize so that the source material will reach and grow on the substrate. Shadow masks are used to create the desired tunnel junction structures without breaking vacuum. Figure 4.1.2 is the schematic for the application of a shadow mask. The material will only grow on the areas which are not covered by the shadow mask. The shadow masks are machined out of thin stainless steel sheets.

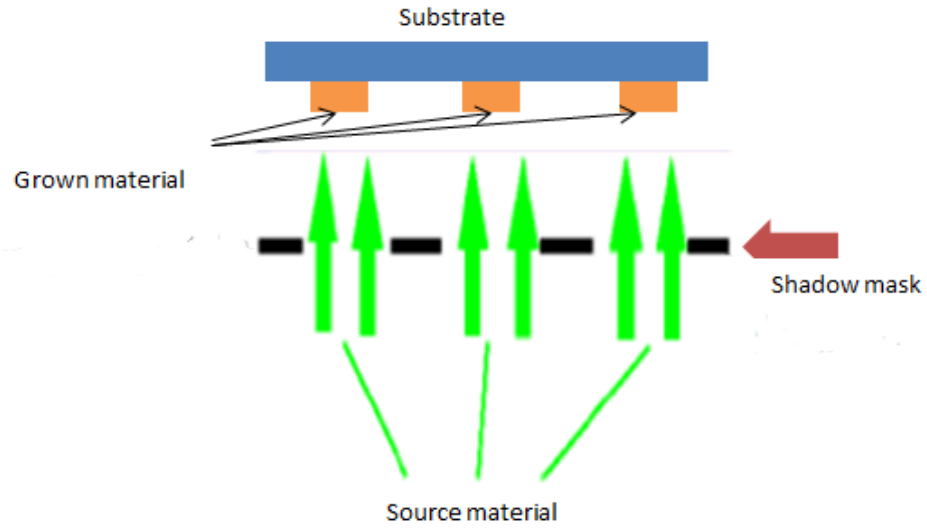

Figure 4.1. 2 schematic structure of shadow mask

4.2 Sample preparation

The sample is grown in the high vacuum chamber with base pressure less than 10^-8 Torr. When the MgO layer is deposited, the system pressure goes into the 10^-7

Torr range which may result in partial Fe oxidation. The growth rate is maintained at 0.1 Å/s for all the layers.

Step 1 Si wafer etch

Si (100) wafer is etched to remove the oxidation using 1% HF.

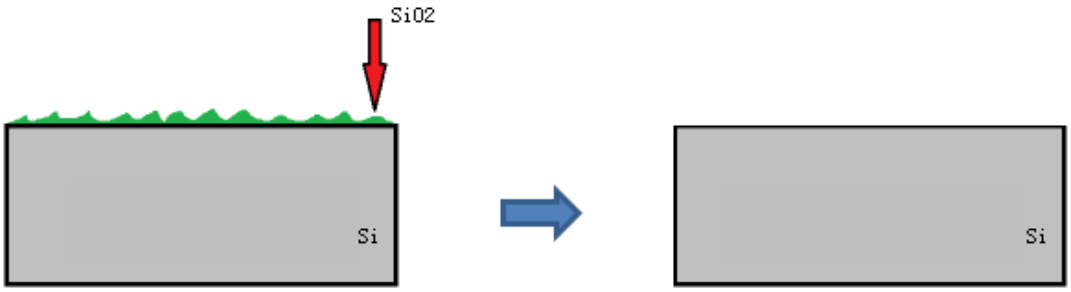

Figure 4.2. 1 wafer etch

Step 2 Buffer layer growth

A 5 nm MgO (100) buffer layer is grown on Si (100) using e-beam evaporation at 300℃ to ensure it is epitaxial.

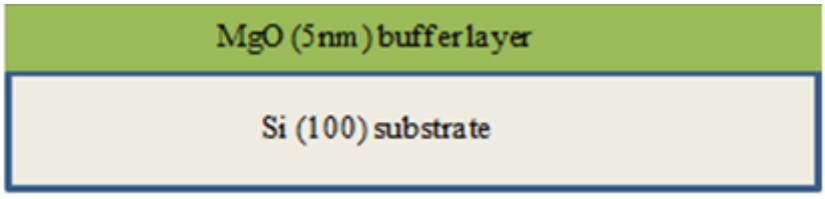

Figure 4.2. 2 MgO (100) buffer layer on Si (100)

Step 3 Bottom electrodes growth

After the buffer layer growth, the sample is cooled down to room temperature. A 7nm Fe (100) bottom electrode layer is epitaxially grown on the buffer layer at room temperature using e-beam evaporation.

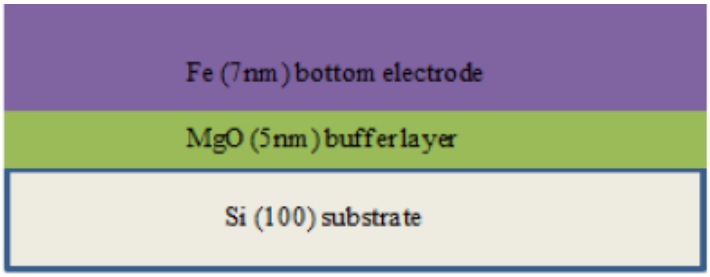

Figure 4.2. 3 growth of Fe (100) bottom electrodes

Step 4 Mg insertion

A 0.7nm Mg layer is grown using thermal evaporation on Fe (100). The substrate is at room temperature. This layer is to protect the bottom electrode from oxidation.

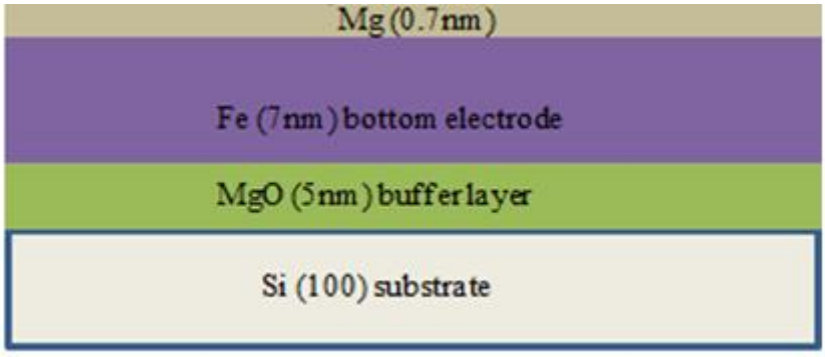

Figure 4.2. 4 Mg insertion

Step 5 Definition layer

The definition layer is formed with 10nm MgO evaporated by e-beam through micro shadow masks. The active junction area is narrowed to 30 μm ×30 μm.

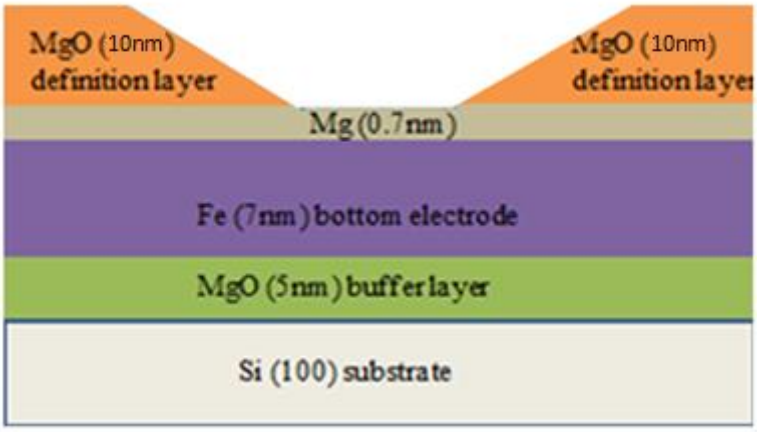

Figure 4.2. 5 Definition layer

Step 6 NaCl Barrier layer

The sample is then heated to 150℃. A 5nm NaCl barrier layer is grown using e-beam evaporation.

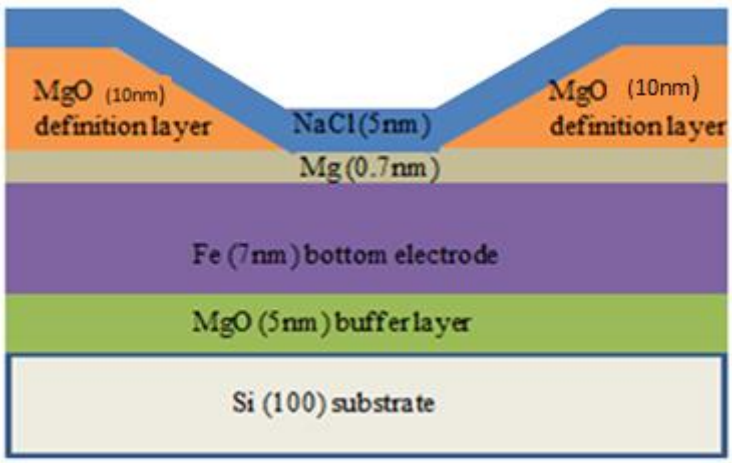

Figure 4.2. 6 NaCl Barrier layer

Step 7 Top electrode Fe layer

A 20nm Fe top electrode is grown at 150℃ using e-beam evaporation.

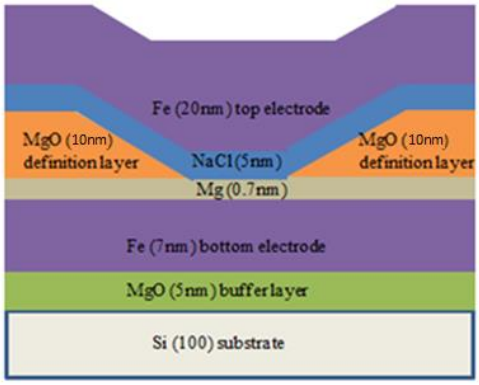

Figure 4.2. 7 Fe top electrode layer

Step 8 Top protection layer

A 20nm Ti is deposited to protect the sample from oxidation and water.

4.3 Measurement

DC transport measurement with four-terminal method is performed on the MTJs. External sweeping magnetic fields are applied at room temperature and 77K. Liquid nitrogen was directly introduced to the sample space and submerged the samples when doing the measurement at 77K. X-ray diffraction is used to measure the orientation of each layer to confirm that the layer is epitaxial.

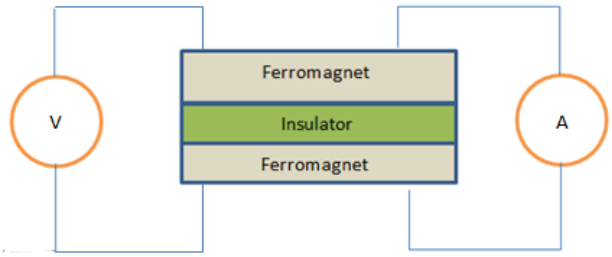

Figure 4.3. 1 The schematic diagram of measurement.

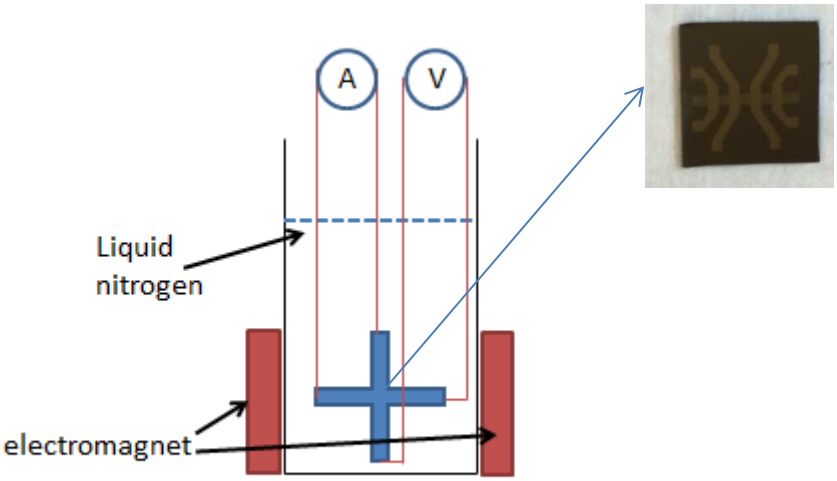

Figure 4.3. 2 The schematic diagram of measurement (in liquid nitrogen).

Chapter 5

Results and Discussions

This chapter will demonstrate the results and the discussion of the experiments.

5.1 Epitaxial growth of NaCl on Fe (100)

Previous results with X-ray Diffraction had confirmed that the MgO buffer layer on Si and the bottom Fe electrode (100) are epitaxial. [11]

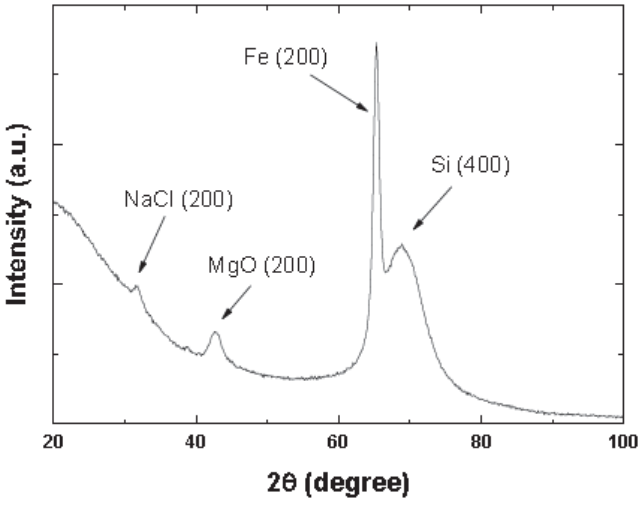

Figure 5.1. 1 XRD θ-2θ scan of MTJ without Mg insertion. To avoid the intense Si (400) diffraction and its satellite peaks, the ω angle was offset by 2.5° in the scan. The

layers' thicknesses are in nm: (100)-Si / 5 MgO / 7 Fe / 3 NaCl / 20 Fe. [49]

When NaCl and top Fe were directly grown on the bottom Fe (100) at 150 ℃, the stack is fully epitaxial as shown in Figure 5.1.1. The NaCl layer is 3nm. And all of materials are in (100) direction.

Additionally, an off-axis ψ scan was performed on the Fe (222) reflections to verify the top electrode is still epitaxial. From previous knowledge, the Fe (100) layers are 45 ° rotated in-plane to the Si substrate [11]. Therefore, to confirm the orientation of NaCl, we fabricated a sample which has epitaxial Fe (100) bottom electrode followed by a 12 nm NaCl layer with Al2O3 capping to protect it from water. The off-axis ψ scan is shown in Figure 5.1.2.

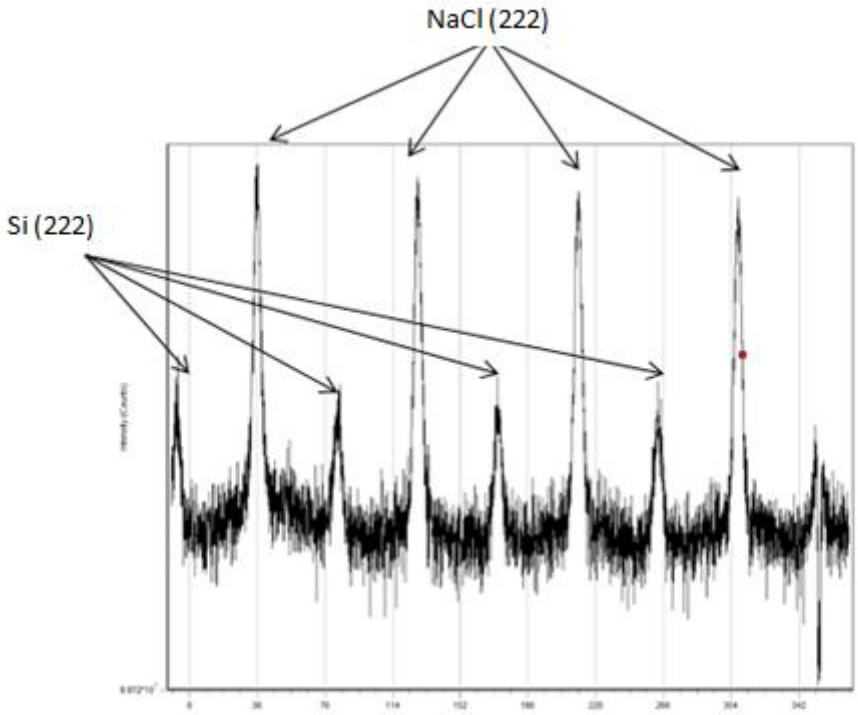

Figure 5.1. 2 off-axis φ scan on the Fe (110) reflections. The layers' thicknesses are in nm: (100)-Si / 5 MgO / 7 Fe / 12 NaCl / 5 Al2O3

The NaCl (222) reflection showed four-fold symmetry under φ rotation. And NaCl lattice is confirmed to be also 45 ° rotated relative to Si, therefore it is aligned

straight with Fe lattices. The bulk lattice parameters of NaCl and Fe are 5.640 Å and 2.867 Å, respectively. The lattice mismatch is only of -1.6% and there is a good epitaxy correlation expected between them.

5.2 Characterizations of Fe/NaCl/Fe MTJs with MgO insertion

Although the NaCl can be epitaxially grown on Fe (100), the island-growth of NaCl on Fe results in a large amount of pinholes through the NaCl tunnel barrier which makes the junctions electrically short. A suitable solution is Mg insertion.

The best TMR obtained was instead on samples with ultrathin (0.7nm) Mg insertion. The Mg layer is actually oxidized into MgO in the definition layer deposition process when the pressure is 10^{-7} torr because the oxygen is released from MgO. This ultrathin MgO layer modifies the chemical property of the surface to make its coverage better with NaCl and also protects the Fe bottom electrode from oxidation.

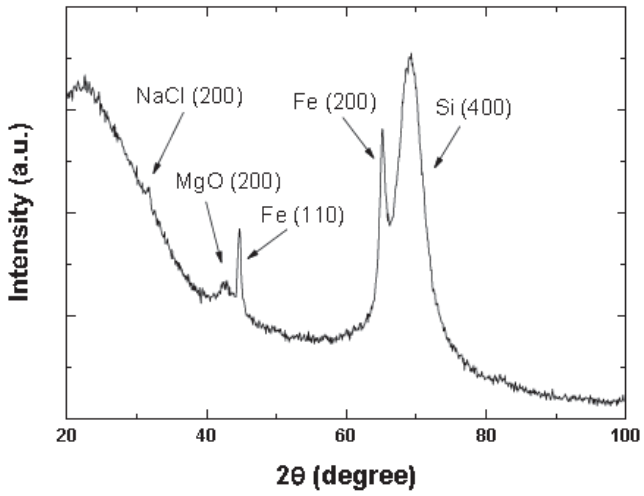

Figure 5.2. 1 XRD θ-2θ scan of the Mg inserted MTJ. The layers' thicknesses are in nm: (100) Si / 5 MgO / 7 Fe / 0.7 Mg / 3 NaCl / 20 Fe. To avoid the strong Si (400) diffraction and its satellite peaks, the ω angle was offset by 2.5 °in the scan. [49]

The concept of Mg insertion process is similar to Tekiel et al [47] using FeO to make NaCl layer by layer growth on Fe. They confirmed the desired growth mode using in situ scanning tunneling microscopy (STM) [50].

While we add the Mg insertion the NaCl barrier and Fe top electrode become polycrystalline. The Fe (110) peak can be observed clearly in the Figure 5.2.1. The Mg interrupted the potential epitaxy correlations with the bottom Fe (100) electrodes. On the other hand it can avoid the pinholes due to the polycrystalline nature of the growth.

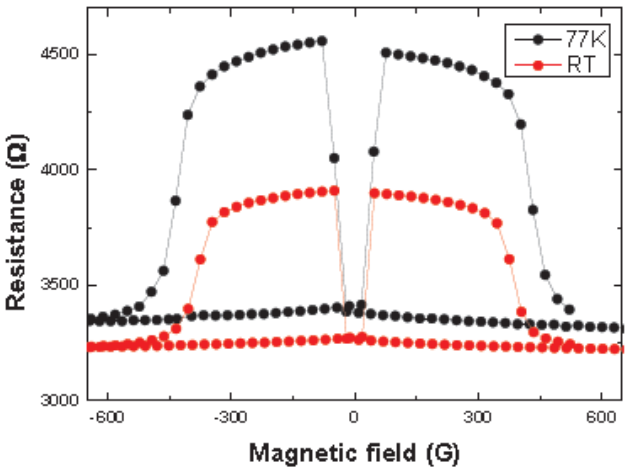

Figure 5.2. 2 Tunneling magnetoresistance measured at room temperature (red) and liquid nitrogen temperature (77K) (black). [49]

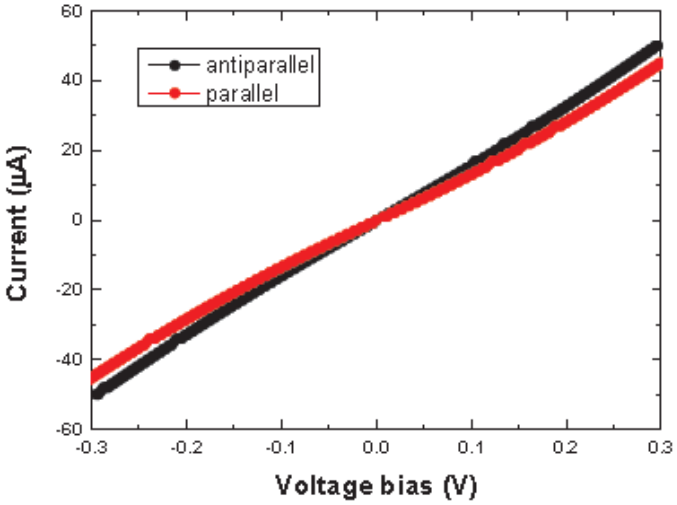

Figure 5.2. 3 The I-V characteristics of the magnetic tunnel junction in its spin parallel (red) and antiparallel (black) configurations at room temperature. [49]

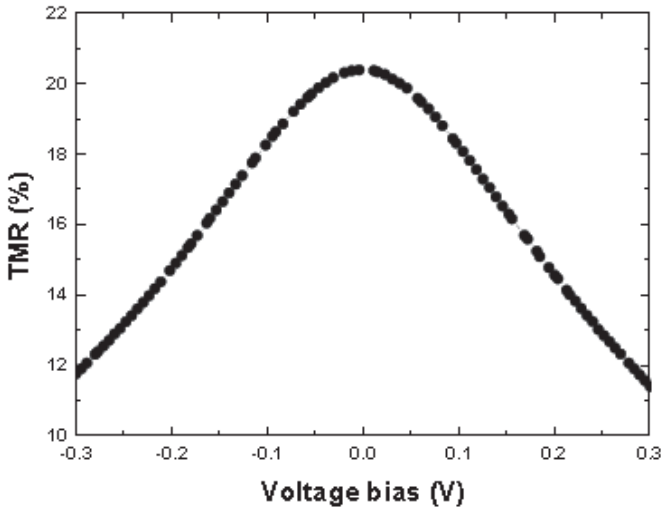

Figure 5.2. 4 Tunneling magnetoresistance ratio vs bias voltage at room temperature [49]

The magnetoresistance curve of the poly-NaCl barrier MTJ is shown in Figure 4.2.2. The TMR is 22.3% at room temperature and 37.8% in 77K. The behavior of the device is similar to the standard TMR behavior which has a non-linear I-V curve and the TMR will gradually decrease when the voltage bias increases (Figure 4.2.3). The resistance and magnetoresistance of the junction are very symmetric to the applied voltage which means the barrier's energy profile is not much affected by the Mg insertion. The TMR decreases from 22.3% to 11.8% at 0.3 V. Therefore the TMR V_{half} is higher than 0.3 V. The device is thus suitable for room temperature applications like the MgO MTJs.

5.3 Selected results of other samples

Samples (thickness in nm)	Epitaxial
5MgO-7Fe-10NaCl-5Al2O3 room temperature	No
5MgO-7Fe-10NaCl-5Al2O3 100℃	No
5MgO-7Fe-10NaCl-5Al2O3 125℃	No
5MgO-7Fe-10NaCl-5Al2O3 150℃	Yes
5MgO-7Fe-10NaCl-5Al2O3 200℃	Yes

Table 4.3. 1 The selected results of the epitaxial growth of NaCl on Fe

Samples (thickness in nm)	TMR
5MgO-7Fe-3NaCl (150℃) - 20Fe (150℃)	short
5MgO-7Fe-3NaCl (150℃) - 20Fe (200℃)	short
5MgO-7Fe-3NaCl (100℃) - 20Fe (100℃)	short
5MgO-7Fe-3NaCl (RT) - 20Fe (RT)	short
5MgO-7Fe- 0.5MgO(RT) -3NaCl (150℃) - 20Fe (150℃)	short

5MgO-7Fe- 0.7MgO(RT) -3NaCl (150℃) - 20Fe (150℃)	10%
5MgO-7Fe- 0.7MgO(RT) -3NaCl (100℃) - 20Fe (100℃)	6%
5MgO-7Fe- 0.7MgO(RT) -3NaCl (200℃) - 20Fe (200℃)	8%
5MgO-7Fe- 0.7MgO(RT) -3NaCl (250℃) - 20Fe (250℃)	5%
5MgO-7Fe- 0.7MgO(RT) -3NaCl (150℃) - 20Fe (200℃)	22%
5MgO-7Fe- 0.7MgO(RT) -3NaCl (150℃) - 20Fe (250℃)	14%
5MgO-7Fe- 0.7MgO(RT) -3NaCl (100℃) - 20Fe (200℃)	8%
5MgO-7Fe- 0.7MgO(RT) -3NaCl (150℃) - 20Fe (175℃)	20%
5MgO-7Fe- 0.7MgO(RT) -3NaCl (150℃) - 20Fe (125℃)	15%

Table 4.3. 2 The selected results of the Fe/NaCl/Fe junctions

Chapter 6

Future Work

The surface properties of the NaCl on Fe in this experiment are still not investigated. We could use the newly established ultra-high-vacuum system in our laboratory to check the surface quality of the NaCl barriers. The in-situ Xray photoelectron spectroscopy (XPS), Aeger electron spectroscopy (AES), and UV photoelectron spectroscopy (UPS) are available to check the chemical integrity of each interface. A custom designed vacuum suitcase also allows the samples to travel into a scanning tunneling microscope (STM) measure the surface properties on the atomic scale.

The process of the experiment can still be optimized to make the NaCl barrier layer and the Fe top electrode to be epitaxial, reducing the pinholes and oxidation. A better epitaxy can be achieved by increasing the temperature when growing the layer. However when the temperature increased the pinholes and oxidation will happen. The solution to the pinholes is making the junction smaller. We can use photolithography or electron beam lithography in the future which will significantly reduce the size of the junctions therefore the probability of pinhole formation. The solution to the oxidation is to fabricate the junctions in ultra-high vacuum environment, in which the Fe surface can stay pristine over extended period of time prior to the next layer deposition.

Going into lithography patterning has another advantage. So far we rely on using shadow masks for the junction fabrication, and MgO is used as the insulator between the top and bottom electrodes. We have identified that the junction definition step, which involves 10nm MgO deposition, is the main source of bottom electrode oxidation. By going into micro/nano fabrication, we no longer need the definition

layer and oxidation would be significantly reduced. By using an UHV deposition system the oxidation can be further reduced. Lithography however posts another major challenge to the process. NaCl readily dissolves in water and any step involving water exposure will destroy the device. For that reason we designed the micro shadow mask technique as our first attempt. For the future, we can try to use lithography processes that have no water components throughout, for example, with PMMA (Poly methyl methacrylate) as the resist and MIBK (Methyl isobutyl ketone) as the developer, instead of using the alkaline solution based developers.

The post annealing techniques widely used in MgO junctions are also important consideration for improving the device performance. Forming on amorphous CoFeB electrodes, we could rely on the tendency of NaCl (and similar materials) to form (100) textured growth and create the amorphous/textured/amorphous heterostructure. Annelaing at a suitable temperature crystalizes the interface into matched (100) oriented "local" epitaxy, coherent tunneling is therefore established. So far we have not attempted with annealing on our devices yet.

Further down the road, there are other opportunities in the series of rock-salt materials. For example, LiF has a good lattice matching with the above systems and consists of extremely light elements only. It minimizes the chance of undesired spin scattering and could push the tunneling spin conductance to a new frontier.

References

[1] Meservey, Robert, and P. M. Tedrow. "Spin-polarized electron tunneling." Physics reports 238.4 (1994): 173-243.

[2] Bader, S. D., and S. S. P. Parking. "Spintronics." Annul. Rev. Condens. Matter Phys. 1.1 (2010): 71-88.

[3] Parkin S S P, Kaiser C, Panchula A, et al. Giant tunnelling magnetoresistance at room temperature with MgO (100) tunnel barriers. Nature materials, 2004, 3(12): 862-867.

[4] Yuasa, Shinji, et al. "Giant room-temperature magnetoresistance in single-crystal Fe/MgO/Fe magnetic tunnel junctions." Nature materials 3.12 (2004): 868-871.

[5] Miao, Guo-Xing, Markus Münzenberg, and Jagadeesh S. Moodera. "Tunneling path toward spintronics." Reports on Progress in Physics 74.3 (2011): 036501.

[6] Butler, W. H., et al. "Spin-dependent tunneling conductance of Fe| MgO| Fe sandwiches." Physical Review B 63.5 (2001): 054416.

[7] Vlaic P. Calculated magnetic and transport properties of Fe/Nacl/Fe (001) magnetic tunnel junction. Journal of Magnetism and Magnetic Materials, 2010, 322(9): 1438-1442.

[8] Tao, L. L., et al. "Tunneling magnetoresistance of FePt/NaCl/FePt (001)." EPL (Europhysics Letters) 105.5 (2014): 58003.

[9] Roessler, D. M., W. C. Walker, and Eugene Loh. "Electronic spectrum of crystalline beryllium oxide." Journal of Physics and Chemistry of Solids 30.1 (1969): 157-167.

[10] N. O. Lipari and A. B. Kunz: Phys. Rev. B 3 (1971) 491.

[11] Miao, G. X., et al. "Epitaxial growth of MgO and Fe/MgO/ Fe magnetic tunnel junctions on (100)-Si by molecular beam epitaxy." Applied Physics Letters 93.14 (2008): 142511.

[12] Miao, G. X., et al. "Disturbance of tunneling coherence by oxygen vacancy in epitaxial Fe/MgO/Fe magnetic tunnel junctions." Physical review letters 100.24 (2008): 246803.

[13] Meservey, Robert, and P. M. Tedrow. "Spin-polarized electron tunneling." Physics Reports 238.4 (1994): 173-243.

[14] Mavropoulos, Ph, N. Papanikolaou, and P. H. Dederichs. "Complex band structure and tunneling through ferromagnet/insulator/ferromagnet junctions." Physical review letters 85.5 (2000): 1088.

[15] Tsymbal, E. Yu, and D. G. Pettifor. "Modelling of spin-polarized electron tunnelling from 3d ferromagnets." Journal of Physics: Condensed Matter 9.30 (1997): L411.

[16] Mathon, J., and A. Umerski. "Theory of tunneling magnetoresistance of an epitaxial Fe/MgO/Fe (001) junction." Physical Review B 63.22 (2001): 220403.

[17] Moodera, Jagadeesh S., and George Mathon. "Spin polarized tunneling in ferromagnetic junctions." Journal of magnetism and magnetic materials 200.1 (1999): 248-273.

[18] Moodera, Jagadeesh Subbaiah, et al. "Large magnetoresistance at room temperature in ferromagnetic thin film tunnel junctions." Physical Review Letters

74.16 (1995): 3273.

[19] Mazin, I. I. "How to define and calculate the degree of spin polarization in ferromagnets." Physical Review Letters 83.7 (1999): 1427.

[20] Jansen, R., and J. S. Moodera. "Magnetoresistance in doped magnetic tunnel junctions: Effect of spin scattering and impurity-assisted transport." Physical Review B 61.13 (2000): 9047.

[21] Wolf, S. A.; Chtchelkanova, A. Y.; Treger, D. M. (2006). "Spintronics—A retrospective and perspective". IBM Journal of Research and Development 50: 101. doi:10.1147/rd.501.0101. edit

[22] Spintronics: A Spin-Based Electronics Vision for the Future. Sciencemag.org (16 November 2001).

[23] Baibich, M. N.; Broto, J. M.; Fert, A.; Nguyen Van Dau, F. N.; Petroff, F.; Etienne, P.; Creuzet, G.; Friederich, A.; Chazelas, J. (1988). "Giant Magnetoresistance of (001)Fe/(001)Cr Magnetic Superlattices". Physical Review Letters 61 (21): 2472–2475.

[24] Binasch, G.; Grünberg, P.; Saurenbach, F.; Zinn, W. (1989). "Enhanced magnetoresistance in layered magnetic structures with antiferromagnetic interlayer exchange". Physical Review B 39 (7): 4828.

[25] Julliere M., Tunneling between ferromagnetic films. Physics letters A, 1975, 54(3): 225-226

[26] Duck, Ian, and Ennackel Chandy George Sudarshan. "Pauli and the spin-statistics theorem." (1998).

[27] Zeeman,Pieter, and Maxime Bôcher."Zeeman effect." Nature 55.1424 (1897): 347.

[28] Governale, M., F. Taddei, and Rosario Fazio. "Pumping spin with electrical fields." *Physical Review B* 68.15 (2003): 155324.

[29] Kovalev, Alexey A., Arne Brataas, and Gerrit EW Bauer. "Spin transfer in diffusive ferromagnet–normal metal systems with spin-flip scattering." Physical Review B 66.22 (2002): 224424.

[30] Miao G X, Münzenberg M, Moodera J S. Tunneling path toward spintronics. Reports on Progress in Physics, 2011, 74(3): 036501.

[31] Parkin S S P, Roche K P, Samant M G, et al. Exchange-biased magnetic tunnel junctions and application to nonvolatile magnetic random access memory. Journal of Applied Physics, 1999, 85(8): 5828-5833.

[32] Mavropoulos P, Papanikolaou N, Dederichs P H. Complex band structure and tunneling through ferromagnet/insulator/ferromagnet junctions. Physical review letters, 2000, 85(5): 1088.

[33] Greullet F, Tiusan C, Montaigne F, et al. Evidence of a symmetry-dependent metallic barrier in fully epitaxial MgO based magnetic tunnel junctions. Physical review letters, 2007, 99(18): 187202.

[34] Mather P G, Read J C, Buhrman R A. Disorder, defects, and band gaps in ultrathin (001) MgO tunnel barrier layers. Physical Review B, 2006, 73(20): 205412.

[35] Nozaki, T., N. Tezuka, and K. Inomata. "Quantum oscillation of the tunneling conductance in fully epitaxial double barrier magnetic tunnel junctions." Physical review letters 96.2 (2006): 027208.

[36] Lu, Zhong-Yi, X-G. Zhang, and Sokrates T. Pantelides. "Spin-dependent resonant tunneling through quantum-well states in magnetic metallic thin films." *Physical review letters* 94.20 (2005): 207210.

[37] Niizeki, Tomohiko, Nobuki Tezuka, and Koichiro Inomata. "Enhanced tunnel

magnetoresistance due to spin dependent quantum well resonance in specific symmetry states of an ultrathin ferromagnetic electrode." *Physical review letters* 100.4 (2008): 047207.

[38] Djayaprawira D D, Tsunekawa K, Nagai M, et al. 230% room-temperature magnetoresistance in CoFeB/MgO/CoFeB magnetic tunnel junctions. Applied Physics Letters, 2005, 86(9): 092502.

[39] Miao G X, Chetry K B, Gupta A, et al. Inelastic tunneling spectroscopy of magnetic tunnel junctions based on CoFeB/ MgO/ CoFeB with Mg insertion layer. Journal of applied physics, 2006, 99(8): 08T305.

[40] Moodera J S, Santos T S, Nagahama T. The phenomena of spin-filter tunnelling. Journal of Physics: Condensed Matter, 2007, 19(16): 165202.

[41] Tulapurkar A A, Suzuki Y, Fukushima A, et al. Spin-torque diode effect in magnetic tunnel junctions. Nature, 2005, 438(7066): 339-342.

[42] Hillebrands, Burkard. Spin dynamics in confined magnetic structures II. Springer, 2003.

[43] Ney A, Pampuch C, Koch R, et al. Programmable computing with a single magnetoresistive element. Nature, 2003, 425(6957): 485-487.

[44] Behin-Aein B, Datta D, Salahuddin S, et al. Proposal for an all-spin logic device with built-in memory. Nature nanotechnology, 2010, 5(4): 266-270.

[45] Kudrnovský, J., et al. "Ab initio theory of perpendicular magnetotransport in metallic multilayers." Physical Review B 62.22 (2000): 15084.

[46] Freeman, A. J., and Ru-quian Wu. "Electronic structure theory of surface, interface and thin-film magnetism." Journal of magnetism and magnetic materials 100.1 (1991): 497-514.

[47] Tekiel A, Topple J, Miyahara Y, et al. Layer-by-layer growth of sodium chloride overlayers on an Fe (001)-p (1 × 1) O surface. Nanotechnology, 2012, 23(50): 505602.

[48] Nakazumi M, Yoshioka D, Yanagihara H, et al. Fabrication of magnetic tunneling junctions with NaCl barriers. Japanese Journal of Applied Physics, 2007, 46(10R): 6618.

[49] Ji Y T, Li Q, Tang Y C, et al. Epitaxial growth of NaCl on Fe (100) and characterization of Fe/NaCl/Fe magnetic tunnel junctions//Nanotechnology (IEEE-NANO), 2014 IEEE 14th International Conference on. IEEE, 2014: 594-597.

[50] Chen C J. Introduction to scanning tunneling microscopy. Oxford University Press, 2008.